Review of biomimetic flexible flapping foil propulsion systems on different planetary bodies

Naga Praveen Babu Mannam [a], Md. Mahbub Alam [a,*], P. Krishnankutty [b]

[a] Center for Turbulence Control, Harbin Institute of Technology, Shenzhen, 518055, China
[b] Department of Ocean Engineering, Indian Institute of Technology (IIT) Madras, Chennai, 600036, Tamilnadu, India

ARTICLE INFO

ABSTRACT

Locomotion techniques employed by different biological animals are extremely diverse and fascinating from an engineering point of view. The explorations of planets such as Mars, Titan, Europa, Enceladus with the use of aerial, terrestrial, and underwater rovers are gaining significant interest from academia, industry, planetary scientists, robotic engineers, and international space agencies around the globe. This article presents an overview of the existing state-of-the-art investigations on recently developed flapping foil propulsion of UAVs (unmanned aerial vehicles) and AUVs (autonomous underwater vehicles) for the exploration of Earth's oceans and other terrestrial bodies such as Mars, Jupiter's moon Europa, and Saturn's moon Titan. The use of flapping foils further advances into Martian Atmospheres in the form of insect-inspired micro aerial vehicles working at low Reynolds numbers. The development of aerial vehicles mimicking insect flapping is essential in low Reynolds number environments to generate sufficient lift and thrust for carrying out future Mars missions. The Cassini mission to Titan, Voyage mission, and other flyby missions to Europa found that liquid atmosphere exists on the subsurface of Europa and on the surface of Titan in the form of liquid methane lakes. The ice-covered ocean under the Europa surface is analogous to the Antarctic ice. The developments of autonomous surface ships and underwater vehicles for the exploration of the planets in cryogenic conditions are discussed with suitable biomimetic propulsion systems. The design methodology, hydrodynamic stability, and resistance estimation in cryogenic atmospheres are presented which can act as a benchmark for future missions.

1. Introduction

Biological propulsion in nature is extremely diverse, ranging from the locomotion of microscopic bacteria to majestic eagles and humpback whales. The locomotion through fluid mediums (water and air) is achieved by accelerating the surrounding fluid in the opposite direction [1]. The energy used to accelerate the fluid comes from food, environment, or some other forms of energy stored in living beings. The biological locomotion techniques are fascinating and are employed in various engineering applications [2]. Although the diversity of biological locomotion is very wide, the major modes of locomotion in living beings (excluding microscopic organisms) can be broadly classified into flapping and jetting modes. The flapping mode is the most commonly used locomotion in fish and birds, whereas the jetting mode is observed in ocean squids, jellyfish, and scallops, producing high thrust and easy maneuvering. The flapping wings of living beings are used as a device to produce propulsive forces and to stabilize and control the motion.

Biomimetic propulsion due to its higher efficiency renders a longer operational endurance for marine vehicles. Propellers are used in autonomous underwater vehicles (AUVs), good for surveillance and security, as the propellers provide low disturbance. Biomimetic propulsion systems are also being considered for applications to remotely operated vehicles to be used in the liquid ocean on Europa (the fourth-largest moon of Jupiter) and Titan (the biggest moon of Saturn). Biomimetically propelled AUVs are to be used for earth's ocean observations to find natural resources on the seabed and to conduct rescue and search operations like ship wreckage, flight data recorders, underwater pipeline inspection, offshore structure health monitoring, biological studies in the oceans, etc. Autonomous surface vehicles (ASVs) and underwater vehicles such as AUVs and ROVs (remotely operated vehicles) are extensively used for marine exploration, survey, surveillance, and security. Conventional screw-type propellers are generally used in these marine vehicles [3–5]. However, the noise and disturbances created by this type of propellers may often interfere with the useful ocean data signals. The low

---

Fig. 1. Types of underwater vehicles. (a) autonomous underwater vehicle, (b) remotely operated vehicle, and (c) biomimetic underwater vehicle [108].

efficiency of the screw propulsors is another concern where the endurance of the vehicle operation is brought down. The application of biomimetic propulsion systems to marine vehicles has attracted the attention of researchers to address and solve the above-mentioned problems [6–8]. Typical examples of the above-mentioned underwater vehicles are shown in Fig. 1. These autonomous vehicles are usually small in size, but sufficient to carry out the required experiments with a reduced risk of collision between ships and offshore structures. Small rotary propellers driven by electric motors propel these vehicles. These propellers have low efficiency, low vehicle controllability, high noise signature, and serious time lag in transient state conditions. They are therefore used for short-term missions. In nature, aerial (e.g. birds) and aquatic (e.g. fishes, turtles, and penguins) animals operate at high propulsive efficiencies, having high maneuverability with the help of their bodies and fins. The advantages of bio-inspired propulsors compared to man-made propulsors are described in Sec. 1.1. The underwater robots operating with a bio-inspired propulsion system have shown better performance than those operating with a screw propeller. This superior performance of biomimetic propulsors results in efficient cruising, maneuverability, and low noise motion of the underwater vehicles. The robots are fish-like body, propelled using oscillatory or undulatory motions of either body or fins or both [9]. The applications of bio-inspired propulsion systems are listed in Sec. 1.2. A brief introduction to planetary bodies (e.g. Earth, Europa, Titan where a liquid atmosphere exists) and their physical properties of the fluid are presented and discussed in Sec. 1.3.

1.1. Advantages of bio-inspired propellers over screw propellers

- The propulsion system for tuna fish, mackerel, whale, and dolphin is up to 80% efficient, while the conventional screw propeller is only 40%–50% efficient [10].
- Bio-inspired propulsors act not only as propellers but also as maneuvering devices, and motion stabilizers [11].

- Bio-inspired propulsors feature the absence of cavitations and reduction of wake signature, whereas screw propellers create strong jets and have higher chances of cavitations [12].
- Biomimetic flapping foils are eco-friendly, whereas conventional propellers or turbines damage the marine flora and fauna [13].
- Bio-inspired propulsors produce very low noise signatures compared to the conventional propellers [116]. Hence, the bio-inspired propulsors are highly useful in stealthy operations and are undetectable to synthetic aperture radar (SAR).

1.2. Applications of bio-inspired propulsion systems

- Space: bio-inspired propulsion system is being considered for vehicles to explore the liquid oceans in Europa and Titan [14]. Biomimetic planetary rovers are also planned for operation in Mars atmospheres [15].
- Aerospace: unmanned aerial vehicles in dual media (e.g. air and water), such as flying fish and diving birds [16,17].
- Renewable energy: flapping foils are being used to extract wave and tidal energy [18].
- Marine applications: propelling, stabilizing, and maneuvering devices for ships and underwater vehicles [19,20].
- Floating marine mobile buoys for oceanographic studies [21].
- Biomedical applications: biomimetic nanorobotic devices for drug delivery applications [22].

In the last two decades, research focus has been given on the design and development of biomimetic autonomous underwater robots. The first biomimetic swimming robot was inspired by tuna fish, called Robo tuna built at MIT [23]. Based on the Robo tuna, Vorticity Controlled Unmanned Undersea Vehicle (VCUUV) was developed with advanced developments and capabilities such as avoiding obstacles and having flapping motion [24,25]. Besides this, the existing bio-inspired fish robots have deficiencies in swimming and maneuvering capabilities. The
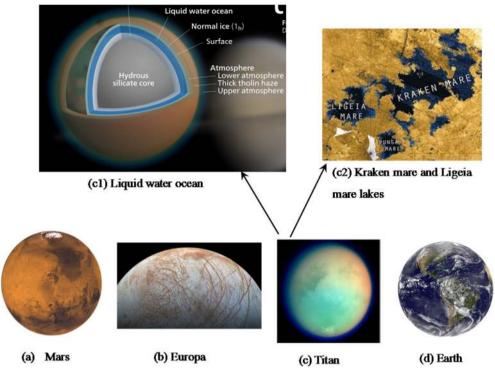
Fig. 2. Planetary bodies [27].

Table 1
Physical properties of planets in comparison with Earth parameters.

	Mars	Jupiter	Titan	Earth
Mean Radius *(km)*	3390	69,911	2575	6371
Gravity *(m/s²)*	3.26	24.79	1.354	9.82
Atmospheric Temperature (° K)	214	165	94	288.2
Atmospheric Pressure *(Pa)*	636	200,000	149,526	101,300
Atmospheric Density, $\rho(kg/m^3)$	0.0155	1326	5.55	1.23
Atmospheric Gases	CO_2 95%	H_2 89%, He 10%	N_2 65–98%	N_2 78%
	N_2 2.7%	CH_4 0.3%,	Ar < 25%	O_2 71%
	Ar 1.6%	NH_3 0.026%	CH_4 2–10%	
	O_2 0.1%	HD 0.0028%		
		C_2H_6 0.006%		
		H_2O 0.0004%		

present work deals with the design and development of bio-inspired propulsion systems for surface ships and underwater vehicles. A comprehensive review of the literature is done here, covering propulsion modes of different biological systems and recreation of fish as underwater robots.

1.3. Planetary exploration

The liquid atmosphere subsists around the Earth, Europa, Titan, and other anonymous celestial bodies such as neutron stars, Gliese 581 d [26]. The photographs of Earth, Mars, Europa, and Titan are shown in Fig. 2a-d, displaying major features around them. Liquid oceans are present beneath the ice crusts of Europa (Fig. 2b). Liquid seas (includes methane and ethane) exist on Titan (Fig. 2c1). The Kraken Mare on Titan is only a well-known body with stable liquid seas in the solar system (Fig. 2c2). It has a spread of 1170 km in width and an estimated depth of 300 m, and its size is similar to that of the Caspian Sea. Ligeia mare lake measures 500 km in width (Fig. 2c2). This is the proposed site for landing

on Titan [27]. The space probe for collecting the samplings on Titan is fitted with a propeller. The main purpose of this space probe is to study the liquid on the moon and to take scientific measurements while sailing.

The physical properties of the planets are given in Table 1. The gravitational acceleration on Mars is about one-third of that on Earth. The atmospheric density on Mars is only 1.3% of Earth's atmospheric density. This low-density atmosphere on Mars results in low operational Reynolds numbers $Re = 10^2$-10^3 for fixed-wing and rotary aircraft which produces insufficient lift. Similarly, in Titan conditions, the *Re* of Titan submarine is 10^5 while the conventional submarine *Re* is 10^9 on Earth.

Space exploration is the exploration and revelation of celestial bodies, planets, and moons. Human spaceflight and unmanned robotic probes (rovers) are used to carry out the physical exploration. The rovers can also be called as planetary rovers, as the name suggests. They are planetary exploration vehicles designed to move across the planet's surface or the celestial bodies. These rovers can be semi-autonomous or fully autonomous. The collection of rock samplings, dust, and images of the surface is the main function of the rovers. When compared to stationary landers, planetary rovers are advantageous as the observations at a microscopic level can be made. Physical experimentations can be conducted, and more territory examination can be done using planetary rovers. However, conventional rovers have limited powering aspects and obstacle avoidance. They have difficulties to maneuver in highly rough terrains, lacking the capability to withstand in harsh environments. On the account of drastic environmental conditions, existing rover systems may not be suitable for exploration.

The inspiration behind the designing and building of the novel and high performance biomimetic planetary rovers for land and liquid atmospheres on planets comes from the plants and animal species evolved in nature. Recent scientific discoveries created interest in exploring Titan and Europa. The conventional planetary rover is wheel operated, designed to operate on firm ground, and proven to be successful in the exploration of the Martian environment. Conventional wheel-type rover designs are inconvenient in a liquid environment as the medium of operation on Europa is either liquid or dense gaseous. To explore liquid atmospheres on Europa or Titan, the rover should be able to propel and
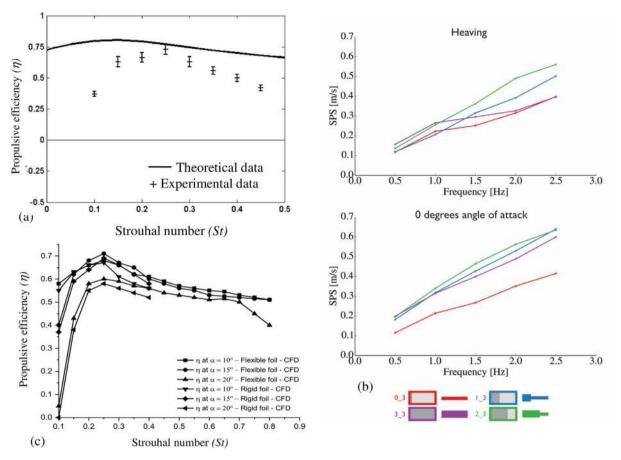
Fig. 3. (a) Propulsive efficiency *(η)* of flapping foil as a function of Strouhal number *(St)* [35]. (b) Self-propelled speeds (SPS) of swimming foils (0_3 – single layer low stiffness material, 3_3 – triple layer high stiffness material, 1_3 and 2_3 – the anterior 1/3 and 2/3 of foil contains high stiffened material) [36]. (c) Propulsive efficiency of flapping foil [37].

maneuver within liquid media effectively, and the operational requirements must be satisfied by the design.

In this work, planetary rover concepts are designed and explained based on biological species living in liquid environments on Earth (e.g. aquatic fish). In the first phase, an extensive literature study is carried out on marine vehicles fitted with flapping foil propulsion systems. The experimental, numerical, and theoretical studies are highlighted in Sec. 2. In nature, the aerial birds and aquatic animals use similar flapping wing/foil concepts for its locomotion. The flapping foils operating in a dual medium are scarcely studied in the literature. Aquatic birds such as guillemot, flying fish, and flying squids use their pectoral fins for flying and caudal fins for underwater propulsion. The experimental studies of flapping foils operating in a dual medium are discussed in Sec. 3. The studies carried out in Secs. 2 and 3 (flapping foils in water and combinations of two fluids) are useful in building the rovers for planetary body exploration which consists of air and water of low densities. In Sec. 4.1, the developments of flapping wing based aerial vehicles for Martian conditions are presented and discussed. The equations of motion for an insect-based flapping wing and aerodynamic forces are also presented. In Sec. 4.2, the presented are the design of bio-inspired surface and underwater vehicle methodologies (such as the selection of geometry) and different stability aspects (vertical, transverse, and longitudinal directions), including stability during surface and diving conditions and stability when surfacing through the ice. The resistance aspects of surface and underwater vehicles operating in Titan conditions are also addressed. In Sec. 4.3, the estimation of resistance of marine vehicles operating in the icy atmospheres of Europa, similar to that of vehicles operating in Antarctic conditions, is presented. Overall, this paper reviews the design of marine vehicles for the exploration of planetary

bodies. Based on this review, the preliminary estimates of hydrodynamic stability, resistance, and powering requirements of the vehicles operating in Titan and Europa can be carried out in future studies. The design and analysis of a biologically inspired or biomimetic rover concept are highly robust and capable of generating thrust with caudal fin and auxiliary (pectoral) fins. These fins increase the efficiency aspects of the vehicle in liquid environments and eliminate the need for rudder devices for maneuvering. The behavior of conventional propellers operating in the cryogenic conditions is still unknown, and the problems associated with propeller cavitation at −180 K are unpredictable.

2. Hydrodynamics of flapping foils for exploration of oceans on earth

The formulation and progress of research in the area of biomimetic propulsion systems for marine vehicles depends on a thorough understanding of its basics as well as the advances in the area. The study of biomimetic propulsion systems gained more importance with the development of new generation autonomous surface ships and underwater vehicles. The controllability of these vehicles becomes more difficult and challenging when they operate in shallow/restricted waterways. The urge for a more precise prediction of the hydrodynamics of autonomous marine vehicles, even at their early design stage, requires a lookout for better numerical ways to study the problem. In this section, the literature are systematically reviewed, presented, and analyzed consistently.
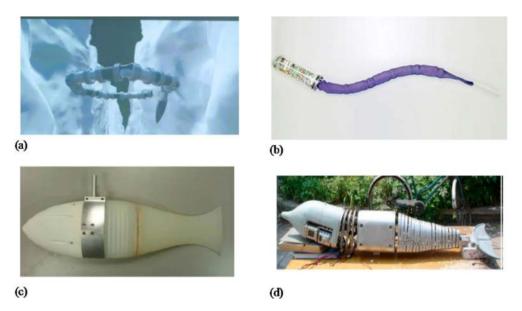
Fig. 4. Bioinspired underwater vehicles. (a) EEL fish robot [45], (b) Lamprey robot [46]), (c) Trout robot [115], and (d) Dolphin robot [47].

2.1. Single foil work

Self-propulsion tests involve model testing where the ship model is moved using the thrust produced by its propulsor. The thrust produced is contingent on the ship model speed. When the model is held to a position and the propulsor is put into the operation, the working condition is termed as a bollard pull test. Morikawa et al. [28] conducted a series of experimental studies on oscillating wing propulsion systems. Under the assumption of quasi-steady flow, a two-dimensional oscillating wing was analyzed. The flow characteristics of and thrust generated by the oscillating wing were obtained using experimental and theoretical approaches. Resembling a dolphin caudal fin with heave motion, the oscillating wing propulsion system, fitted at the bottom of the ship hull, results in a good propulsive efficiency (around 60%) and generates less turbulence. Dewar et al. [29] studied swimming kinematics of a yellowfin tuna in a large water tunnel at controlled swimming velocities. They quantified the kinematic parameters, including caudal fin frequency, amplitude, yaw angle, propulsive wavelength, propulsive wave speed, and pectoral fin angle. All the variables, except propulsive wavelength and propulsive wave speed, were comparable to those determined for other teleost fishes. Koochesfahani [30] carried out extensive research on NACA0012 foil pitching about its quarter-chord location. At a small pitch angle ($\approx 2°$), an increase in the oscillation frequency leads to a change in the von Karman vortex street such that all vortices nestle around the wake centerline, forming a jet. The jet strengthens with the frequency increase [1]. Jones et al. [31] made a comparison between experimental and numerical results for a plunging foil. Different vortex sheddings were observed under a variety of thrust and drag producing conditions. Haugsdal [32], in the MIT Towing Tank performed experiments on a NACA0014 foil oscillating in pitch and heave motions. Some tests to determine the thrust coefficient and propulsive efficiency of the foil were conducted over a large parametric space. The Strouhal number ranged from 0.10 to 0.80, and the maximum attack angle varied between $10°$ and $35°$. The actual efficiency including drag obtained from the experiments was 0.67. Das et al. [33] performed numerical studies on the thrust of a NACA0012 foil pitching about its quarter-chord location from the leading edge with an angular oscillation amplitude of $5°$ over a Strouhal number (*St*) range of 0.2–0.45 and a Reynolds number range of 10–2000, using a high-resolution viscous vortex particle method. The results showed a sharp increase in the maximum propulsive efficiency ranging from 1.7% to 16% at $St = 0.45$ when *Re* is increased from 50 to 1000, and the wake is modified from reverse von Karman street to the deflected wake. Walker and Westneat [34] experimented to understand the locomotion of *Gomphosus varius,* one of the species that use oscillating pectoral fins for maneuvering and propulsion. They observed that the fin of *Gomphosus varius* oscillates largely up and down in a slightly inclined figure-eight pattern with respect to the body. Both oscillation frequency and amplitude of the pectoral fin linearly increase with swimming speed. Alam and Muhammad [1] examined a hydrofoil pitching at $Re = 150$ for $St = 0.1$–0.3 and found that thrust enhances when oscillation amplitude and/or frequency are increased.

Morikawa et al. [38] developed the outboard oscillating wing propulsor using a simple crank mechanism designed to perform heaving and pitching motions. Experiments were carried out to determine the propulsive performance of the wing fitted at the bottom of the hull of a small boat. The propulsive efficiency obtained was greater than 65%. The effects of Strouhal number and angle of attack on the thrust force and hydrodynamic efficiency of the flapping foil were investigated by Schouveiler et al. [35]. The propulsive efficiency of the flapping foil was reported as more than 70% for the optimal combination of the kinematic parameters (Fig. 3a). Gottlieb et al. [39] studied the pectoral fin model of bluegill sunfish during its maneuvering to avoid the obstacles. This study involves biological studies of pectoral fins of sunfish, developing kinematic models of the motion of pectoral fins. The robotic fin produced the forces for swimming and maneuvering with high performance. Lauder et al. [40] studied some of the key features of the mechanical design of a robotic fish and then focused on the mechanical design of fin rays that allow active muscular control of curvature and flexibility of the fish body in propulsion. Shinde et al. [41] performed an experimental study on purely pitching foil with a flexible flap of various stiffness values. The rigid pitching foil produces a weak and meandering jet whereas the flexible foil produces a strong jet in the wake. Deformations of the flexible flap (bending stiffness EI $= 3.15 \times 10^{-7}$ Nm^2, 0.05-mm thick polythene sheet) suppress the meandering by increasing the initial gap between two successive vortices and by imposing a convective motion on the shed vortices even in the absence of the freestream velocity. Lucas et al. [36] studied a fish model with varied stiffness (EI $= 5.5 \times 10^{-5}$ Nm^2 to 1.9×10^{-5} Nm^2) in the spanwise direction of biologically relevant magnitudes. The forces and torques in the three directions (*x,y,z*) and the swimming performance under both heaving and pitching motions were experimentally examined at an attack angle of $0°$, $Re = 21,000$ - 115000 and $St = 0.2$–0.45. The foils of non-uniform stiffness gave a high propulsive speed (Fig. 3b) [115]. Young et al. [42] studied the unsteady
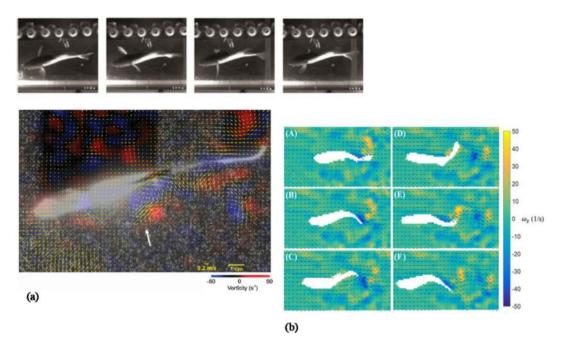
Fig. 5. (a) PIV analysis of bluegill sunfish swimming backwards raw image (top row) and Anal fin vortices (second row) [57]. (b) Zebrafish swimming in cruising mode [58].

forces acting on NACA0012 rigid heaving foil inspired from the sail dynamics at $Re = 10,000$, $\alpha = 0°–20°$ and reduced frequency of 1.6–3.2. The results showed that the mean lift force is six times greater than that on the static foil and two times greater than that on foil with the classical heave motion.

2.2. Multiple foil work

Lua et al. [43] experimentally and numerically studied 2D flapping foils in a tandem configuration for the forward propulsion at $Re = 5000$. Both tandem foils were subjected to symmetrical translational and rotational motions with $St = 0.32$. The results showed that the foil-wake interaction is favorable to thrust generation when the downstream foil crosses the shear layer from the upstream foil. A ship model experiment with a pair of flexible flapping foils, made of polyurethane, achieved a propulsive efficiency of 55% [113]. Mannam et al. [37] studied the self-propulsion and bollard pull characteristics of the ship model furnished with tandem foils where the foil operates in sway and yaw modes. The analysis was carried out for $St = 0.1–0.85$, and the maximum efficiency of 73% was achieved at $St = 0.225$ (Fig. 3c). Bowker and James [44] carried out experimental studies on submerged flapping foils to convert wave energy into ship propulsion. Submerged foils were able to capture wave energy for onboard power generation and for a self-propelling vessel. A maximum vessel speed of 0.48 m/s at a wave frequency of 5 Hz was achieved in head sea conditions. Similarly, in the following sea conditions, a maximum vessel speed of 0.72 m/s was observed at a wave frequency of 6 Hz. Furthermore, the experimental and numerical studies concluded that the submerged foils can generate thrust force from the ocean waves.

Some of the underwater vehicles for the exploration of Earth and other liquid planetary bodies are shown in Fig. 4. The ongoing research on developing bio-inspired underwater vehicles for the exploration of Saturn's moon Enceladus and Earth's oceans is presented here.

Eel fish robot for Saturn's moon Enceladus: The vehicle consists of a slender body with the head acting as fulcrum (Fig. 4a), equipped with all sensors for carrying out scientific studies on Saturn's moon Enceladus [45]. Using pressure sensors, the robot autonomously follows the terrain and reconfigures itself based on the reactive forces. The vehicle tail is fitted with an anchor. It works in anguilliform mode.

Lamprey robot for Earth's ocean: This lamprey robot consists of a rigid head, a flexible body, and a passive tail (Fig. 4b). The robot is actuated by artificial muscles made of a shape-memory alloy [46]. The actuation of these muscles in sequence provides the rhythmic lateral undulations, which generates the swimming motion of the robot. The robot could propel backward by reversing its rhythmic undulation. It also works in anguilliform mode.

Trout robot for Earth's ocean: The trout body has mainly three parts such as a nose cover, a middle flange, and a silicone tail [115]. The electronics and actuation components are inside the nose cover and the flange (Fig. 4c). The propulsion is made in the posterior part of the robot using a rotational actuator. A sinusoidal rotation of the motor causes undulation of the tail to propel the robot. It works in a subcarangiform mode.

Dolphin robot for Earth's ocean: Yu et al. [47] developed a five-link dolphin robot that was actuated by using five DC servo motors (Fig. 4d). To further increase the efficiency, the two motor-driven scotch yoke mechanisms are used for the tail undulation. It works in a carangiform mode.

2.3. PIV studies on swimming fish

Van Duren et al. [48] measured the flow around an adult copepod at Reynolds numbers less than 100 and computed the vorticity fields. Muller et al. [49] carried out PIV studies on a freely swimming mullet in a horizontal plane. The body of the mullet was identified manually in each frame. They also observed the sign of opposite vortices in the wake of the fish body. Wolfgang et al. [50] performed PIV studies on a freely swimming giant danio and measured the flow in the horizontal plane. They observed vortex shedding around the tail fin during straight-line swimming and turned maneuvering. Hanke et al. [51] studied the swimming behavior of goldfish (60 and 100 mm body length) and observed the water disturbances caused by the goldfish. The disturbances developed like vortex ring-like structures leaving the tail of goldfish. Sakakibara et al. [52] carried out three-dimensional velocity measurements on a freely swimming goldfish. During a turning circle maneuver, side jets are produced in the counter-rotating vortices of the fish body. Matsuuchi et al. [53] used stereoscopic PIV for capturing three velocity components on live goldfish along with particle tracking velocity to determine spatial
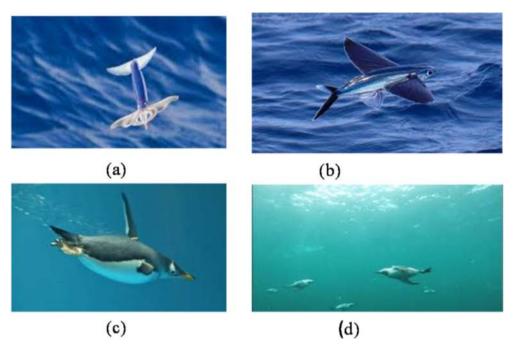
Fig. 6. Photographs of creatures operating in both air and water. (a) Flying squid, (b) flying fish, (c) penguin, and (d) guillemot.

velocity, acceleration, and vorticity. Tytell and Lauder [54] using PIV carried out an experimental study on an anguilliform eel fish swimming steadily and observed the wake flow characteristics. It was observed that for every tail beat two vortices of opposite signs are created. Warrick et al. [55] conducted PIV studies on aquatic animals and estimated the locomotor forces during swimming. Recent developments in flow visualization methods enable the researchers to realize direct visualization of flow in the animal wake through the measurements of velocity and vorticity fields. These data are necessary for estimating the propulsive forces in the wake of the animal. Lauder [56] studied three-dimensional interactions of swimming as it is a critical analysis for engineers and biologists. These studies can be extended to the development of bio-mimetic robotic vehicles, mainly in determining the primary and secondary fin configurations of the vehicles. Mannam et al. [113] carried out flow visualization experiments on hydrodynamic aspects of fish locomotion and maneuvering using a 2D PIV system. The caudal fin of the freshwater shark produced Karman and reverse Karman vortex streets. The amplitude and frequency were the main responsible factors for the production of reverse Karman vortices that enhance the thrust [1]. Flammang and Lauder [57] using PIV studied the bluegill sunfish having multiple flexible fins (control surfaces) that help in swimming backward and turning without changing the body position. The bluegill sunfish swimming backward (raw image) is shown in Fig. 5a. The PIV analysis of the anal fin shows that anal fin producing jet towards the anterior posture (near to fish head) is responsible for backward swimming. Mwaffo et al. [58] studied the flow physics around the zebrafish swimming in uniform currents in a water tunnel using PIV. This study examined the role of flow speed on tail beat amplitude, swimming speed, and heading direction. When compared to the bursting mode of swimming, the magnitude of body bending and tail oscillation in cruising mode is very small. A complete cycle of the tail beat is shown in Fig. 5b, where the fish direction is relatively steady over time. The vortices of alternating signs are shed from the tail, moving downstream throughout the swimming.

3. Development of flapping foils in dual (air and water) mediums

The development of flapping foils advances to dual mediums (e.g. air and water) of two different densities. The inspiration came from the flying squids which can swim in water and fly through air, using the jet propulsion mode. Fig. 6 shows some animals operating in both air and water. Flying fish use caudal fin for propulsion in underwater and pectoral fins for flying through the air. Penguins and guillemot birds use pectoral fins for propelling in air and water. The animals operating in either medium use body or wing morphing techniques [59]. The associated experimental and numerical studies in the literature are summarized in Table 2.

The above works presented in Secs. 2 and 3 prove that the experimental approaches have been quite successful in predicting the performance of biomimetic propulsion systems for ships and AUVs. A high degree of robustness and reliability has also been observed in the parametric identification techniques in the design and development of bio-inspired systems for marine vehicles. Other theoretical methods can only give rough estimates of the thrust generated by flapping foils [1]. RANSE based CFD techniques have been successfully employed in the simulation of two-dimensional flow around flapping foils. A confidence level in its application to the three-dimensional flapping foil is yet to be achieved. Researchers are now homing in on the numerical study of three-dimensional flapping foils for marine vehicles. The application of oscillating fins as propellers to conventional marine vehicles is being tested, and this has given the impetus to concentrate on bio-inspired propulsion for marine vehicles. This necessitates the need for the detailed experimental and numerical study of a three-dimensional fish-like propulsion system used in the surface and sub-surface marine vehicles. It is worth understanding the fluid-particle-level movements around different fins during live fish swimming. It is also necessary to test the physical model mimicking the fins and their motion to determine resulting thrust, torque, and propulsive efficiency.

4. Application of flapping foils in planetary bodies such as Mars, Europa, and titan

The exploration of planetary bodies such as Mars, Europa, and Titan received significant interests from space agencies such as NASA, ISRO, ESA, and other commercial entities (e.g. Space X and Boeing). The main objectives of the exploration of these planets are to determine the habitability of the environment, to identify minerals, and to obtain the surface weather measurements. Transportation of humans to Mars is a new challenge to these space research institutes.

Table 2
Studies on flapping wings based on kinematics.

Authors	Flying mode/ investigation approach	Wing kinematics	Investigated parameters	Discussion
Muramatsu et al. [60]	Squids – jet propulsion/ motion camera	Jetting, gliding and diving mode	Lift force	The flight of squid involves jet propulsion, generation of lift force and control of different body postures in different flight phases.
Lock et al. [61]	Guillemot retracted flapping wings/ experimental	2 DOF– roll and pitch	Thrust	Retracted flapping foil produces sufficient thrust at a particular selection of parameters.
Ristroph et al. [114])	Jellyfish/10-cm prototype with 4 flapping wings/ experimental	Opening and closing of the flapping wings like jellyfish.	Lift force	Producing lift and exhibiting stability of the vehicle.
Chen et al. [62]	Insect flapping wing mechanism/ experimental robot	2 DOF – roll and pitch	Lift force	The flapping vehicle successfully demonstrated the different phases of aerial hovering, air-to-water transition, swimming, water take-off, and landing.
Krieg et al. [63]	Squid inspired AUV/ experimental, motion tracking	Jetting	Thrust	The performance of bio-inspired squid thrusters is much more than that of the traditional thrusters. The vehicle performs better in yaw and sway modes.

4.1. Flapping wing aerial vehicles in Martian conditions

The development of conventional aerial vehicles in Mars' atmosphere remains difficult due to the thin Mars' atmosphere with a low density. The gravitational acceleration on Mars is 0.38 times that on Earth while the atmospheric density on Mars is 0.013 times that on earth [64]. As the aerodynamic forces are proportional to ambient fluid density and weight is proportional to the gravitational acceleration, flying on Mars is impossible, given that the ratio of the gravitational acceleration to the density on Mars is 29.23 ($= 0.38/0.013$) times higher than that on Earth. In order to design the flying aerial vehicle on Mars, the following force balance equation between a vehicle's weight and lift should be considered.

$$W = mg_{mars} = \frac{1}{2}\rho_{mars} V^2 S C_L \quad \text{and} \tag{1}$$

$$C_L = C_L(Re, M, k, AR, \alpha), \tag{2}$$

where W is the weight of the vehicle, m is the mass of the vehicle, g_{mars} is the Martian gravitational acceleration, ρ_{mars} is the Martian atmospheric

Table 3
Dimensionless parametric values for insects operating at low Re.

Dimensionless Parameter	Symbol	Definition	Typical values for Insects
Aspect ratio	AR	$\dfrac{R^2}{S}$	2–10
Reduced frequency	k	$\dfrac{\pi f c}{V}$	0.1–0.4
Reynolds number	Re	$\dfrac{VL}{\mu}$	$O(10^2\text{-}10^4)$
Angle of attack	AoA	$\dfrac{\pi}{2} - |\alpha|$	$<45°$
Wingtip Mach number	M_{tip}	$\dfrac{V}{a}$	<0.1
Lift coefficient	C_L	$\dfrac{L}{0.5\rho V^2 S}$	$O(10^1)$

density, V is the velocity, S is the wing surface area, C_L is the lift coefficient, Re is the Reynolds number, M is the Mach number, k is the reduced frequency, AR is the aspect ratio and α is the angle of attack. The definitions of the dimensionless parameters operating in the insect regime are given in Table 3. These parameters are a combination of morphological and kinematic aspects. In Table 3, R is the span of the wing, S is the planform area of the wing, f is flapping frequency, c is the chord length, μ is the fluid dynamic viscosity, L is the reference length, a is the speed of sound. Considering the gravity and density on Mars, conventional fixed-and rotary-wing aerial vehicles generate insufficient lift. Additionally, oxygen is absent in the Mars environment, preventing the use of air-breathing propulsion. The low density also results in low operational Reynolds number in the range 10^2–10^4. To compensate C_L, all the conventional aircraft must fly faster with the smallest wing load capacity.

Several conceptual designs of conventional fixed and rotary wing vehicles were made and developed. The aerial scale environment surveyor (ARES) is a robotic platform, a rocket-powered vehicle which helps in NASA Mars Exploration program [65–71]. This vehicle flies at the altitudes of the Martian environment between 1 and 2 km. The facility of landing on the Martian atmosphere is not possible. This Mars Gas hopper vehicle uses CO_2 propellant for its mobility [72]. To tackle the low-density atmosphere, several free falling concepts and Mars balloons have been proposed [73–75]. The inspiration to achieve flight on Mars is rapidly increasing. NASA Jet Propulsion Laboratory (JPL) is developing Mars helicopters that are designated to fly in the next Mars mission in 2020. This vehicle using rotorcrafts in low densities is limited to fly about 3 min each day [76]. Additionally, the rotor diameter is 1 m, requiring large transport volume in payload vehicles. Despite these potential deficiencies in rotorcraft and fixed-wing vehicle concepts, insect-inspired solutions for lift enhancement may render higher efficiency, robustness, and compactness. Insects, operating at low Reynolds numbers on Earth, are suitable for low Reynolds number environments such as Mars. These insects use unsteady aerodynamic mechanisms and results in a high C_L. The resulting wing motion produces sufficient lift to balance its weight in Martian conditions. Hence, the goal of developing an insect-inspired flight on Mars is still an open problem.

4.1.1. Wing kinematics

The flapping wings of insects operating in low Reynolds number environments use unsteady aerodynamic mechanisms rather than classical aerodynamic theories. Berman et al. [77] described the kinematics of insect flapping wing motion in experimental and computational studies as a sine function of time t, i.e.

$$\zeta(t) = Z\cos(2\pi f t) + \zeta_0, \tag{3}$$

where $\zeta(t)$ represents the wing trajectory, Z is the flapping amplitude, and ζ_0 is the flapping offset angle. The pitch angle α as a rotation away from vertical orientation in the stroke plane is given by
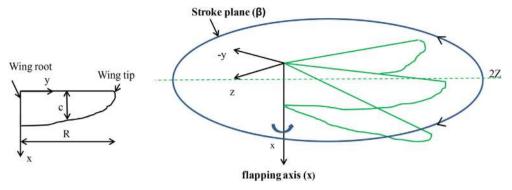
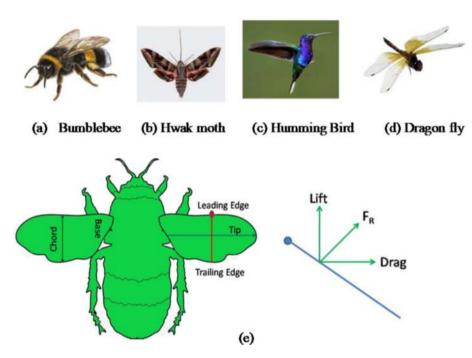**Fig. 7.** (a) Schematic illustration of semi-elliptic insect flapping wing, and (b) flapping motion.

Fig. 8. (a–d) Insect based flapping flight. (e) Aerodynamic forces acting on insect wing element.

$$\alpha(t) = \frac{A}{\tanh(C_\alpha)} \tanh(C_\alpha Sin[2\pi ft - \alpha_\varphi]), \tag{4}$$

where A is the pitch amplitude, α_φ is the pitch phasing angle, and C_α is the coefficient of attack angle. The stroke plane angle β, Z, and ζ_0 are the three input parameters to actuate the three-degree of freedom (3-DOF) system. The semi-elliptic flapping wing subjected to flapping motion is shown in Fig. 7. These parameters control the vertical, horizontal, and angular DOF, respectively [78]. It is necessary to understand how an insect-scale flapping wing produces its aerodynamic characteristics in Martian conditions.

Micro air vehicles (MAVs) using flapping wings have been actively examined in the last two decades, which can revolutionize our capabilities in environmental monitoring, surveillance, and security. While an insect flies, its wings not only move forward but also flap up and down, plunge and sweep, so that both lift and thrust generated can balance its flight. By adjusting the wing speed and effective angle of attack, natural flyers can accommodate uncertain surrounding environments.

4.1.2. Flexible flapping wings of insects

To develop the insect-based flapping wing aerial vehicles in Martian conditions, the challenges are to determine the parameters associated with structures and morphological wings. The insects operating at low

Reynolds numbers are bumblebees, hawkmoths, hummingbirds, fruit-flies, dragonflies, and many others (Fig. 8a–d) which provide the basic information on the starting point of the design for developing inspect-based flying aerial vehicles on Martian conditions [79]. The aerodynamic forces acting on an insect wing element are shown in Fig. 8e. The flow separating from the sharp leading edge of the insect wing element leads to formations of leading-edge vortices. The resultant aerodynamic forces when resolved along and normal to the fluid flow are termed as lift and drag forces. A higher angle of attack leads to an increase in the drag force component. The flapping wing motion of aerial birds consists of down-stroke and upstroke mainly in two-degree of freedom. In the insect regime, the flapping motion of the wing has three-degree of freedom, such as the main flapping wing motion, a slight deviation from the stroke plane, and the active wing rotation. Insects flap their wings in an 8-shaped pattern which results in a generation of unsteady aerodynamic forces. Table 4 summarizes the review of insects flapping wing kinematics and aerodynamic forces. It is observed that the flapping insect flight operating in the low Reynolds number regime generates sufficient lift by considering the wing deformations in both chordwise and spanwise directions. Based on the above studies, the development of micro aerial vehicles, based on bumblebee insects, for Martian conditions are mentioned in Table 5. With the above vehicle parameters mentioned in Table 5, the experiments were carried out in the

Table 4
Studies on insect flapping wings based on kinematics.

Authors	Insect Mechanism	Wing Kinematics	Parameters	Discussion
Cheng and Sun [80]	Liriomyza sativae (fly)	Clap and fling	Vertical lift force	The clap and fling motions increase the lift by 7% compared with no aerodynamic interaction between the two wings. The fly mainly uses the delayed stall mechanism to generate high-lift forces.
Brandt et al. [81]	Fruitfly	Flapping	Vertical lift force	Used 3D realistic wing at $Re = 71$–200 and $\alpha = 10$–$20°$. The corrugations are found in the wingtips at high angles of attack. The corrugations on the wing surface reduce the drag coefficient significantly.
Noda et al. [82]	Hawkmoth	Rigid and flexible revolving flapping wings	Lift and thrust force	During steady rotation, a flexible wing generates more vertical forces at high angles of attack ($\alpha = 40°$–$60°$) while the horizontal force is less than the rigid wing model.
Vargas et al. [83]	Dragonfly	Gliding mode	Vertical lift forces	At low angles of attack, the corrugation of the wing produces circulation and negative shear drag. At high $Re = 5000$, the dragonfly wing produced higher aerodynamic performance than the conventional profile.
Meng and Sun [84]	Insect (saw-tooth approximation)	Gliding mode	Vertical lift forces	The negative induced shear drag was observed during the numerical simulations at $Re = 2400$ and reduces the aerodynamic performance.
Mou et al. [85]	Hoverfly	Inclined 8 - shaped pattern	Resultant thrust force	The thrust force produced is 86% in the downstroke and 14% in the upstroke.
Sun et al. [86]	Dragonfly	Horizontal 8 - shaped pattern	Resultant thrust force	The interaction between the tandem wings reduces the thrust on fore and hind wings by 14% and 16%, respectively, in comparison with the single wing.
Shyy et al. [87]	Bee, hummingbird, wasp, locust, dragon fly, hawkmoth	Clap and fling	Thrust forces	The effective attack angle and thrust forces increase due to wing deformation in the spanwise direction.
Lian et al. [112]	Dragonfly	Pitch-plunge	Resultant thrust force	The backward wing follows phase shift in thrust generation when 90° or 180° phase lag.
Lian et al. [112]	Dragonfly	Pitch-plunge	Vertical lift force	Dynamic motion of the fore flapping wing followed by stationary hind wing reduces the variation inlift forces.
Amiralaei et al. [88]	Flap, airfoil	Inclined 8 - shaped pattern	Vertical lift force	The inclined 8-shaped pattern contributes to the vertical lift force during the upstroke.
Fenelon et al. [89]	Bee	Inclined 8 - shaped pattern	Vertical lift force	The ratio of insect body drag to weight is equal to the ratio of horizontal thrust coefficient to the vertical lift coefficient.
Fujikawa et al. [90]	Butterfly	Flapping	Vertical lift force	The unsteady three-dimensional vortices are mainly accounting for the generation of the lift force.
Sun et al. [86]	Dragonfly	Horizontal 8 - shaped pattern	Vertical lift force	The vertical force of dragonfly insect flapping wing is approximately 35%. The lift coefficient in 3D wing case is 20% less than in 2D case.
Amiralaei et al. [88]	Flap, airfoil	Inclined 8 - shaped pattern	Drag force	The inclined 8-shaped pattern has substantial drag forces, generating required hovering force.
Studies on insect wing structures				
Authors	Insect Mechanism	Wing structure	Lift/thrust/efficiency	Discussion
Du et al. [91]	Hoverfly	Deformable Hoverfly shaped wing	Lift	The increase in lift force for a flexible wing is 10% higher than that of a rigid wing. The increase in lift force is due to camber deformation.
Meng et al. [92]	Insect		Lift	The corrugation of the wing decreases the mean lift by 5%.
Du et al. [91]	Hoverfly		Thrust/efficiency	A deformable wing requires 5% less power than a rigid wing.
Levy et al. [93]	Dragonfly		Drag	The reduction in vorticity reduces the drag.
Experimental studies on developments of prototype aerial vehicles				
Authors	Modes of flight	Wing Shape	Wing span/Re/velocity	Discussion
Fenelon et al. [89]	Hover	Tapered	9 cm, 10 cm/s	The steering mechanism was designed and developed.
Phan et al. [94]	Vertical	Elliptical	125 mm, 10 cm/s	Pitching Stability
Fujikawa et al. [90]	Forward and Vertical	Butterfly	120 mm, 10 cm/s	Motion Analysis during vertical takeoff
Mou et al. [85]	Hover	Hoverfly wing	6.93–9.7 mm, $Re = 240$-330	Wing kinematics and aerodynamic analysis
Numerical studies on developments of prototype aerial vehicles				
Authors	Type of insect/Modes of flight/Geometry/Re/	Numerical Technique	Mesh type	Nodes
Mou et al. [85]	Hoverfly/Hover/3D rigid rectangular/240-330	Navier Stokes	O–H type grid, moving grid system	$100 \times 99 \times 130$ grid points
Orlowski et al. [95]	Corrugated insect wing/Hover/3D rigid/35-3400	Navier Stokes	O–H type grid, moving grid system	$70 \times 110 \times 70$ grid points for corrugated wing and $86 \times 99 \times 114$ for flat wing
Du et al. [91]	Hoverfly/Hover/3D flexible rectangular/800	Navier Stokes	Dynamically deforming grid	$100 \times 90 \times 120$ grid points
Sun et al. [96]	Hoverfly/Hover/3D rigid rectangular	Navier Stokes	O–H type grid, moving grid system	$93 \times 109 \times 78$ grid points
Sun et al. [97]	Bumblebee/Hover/3D rigid rectangular/1326	Navier Stokes	O–H type grid	$71 \times 73 \times 130$ grid points
Sun et al. [86]	Dragonfly/Hover/3D rigid rectangular/1350	Navier Stokes	Moving overset grids, O–H type grid for wings	$29 \times 77 \times 45$ wing grid points, $90 \times 72 \times 46$ background grid points

vacuum chamber of the test section with a diameter of 1.8 m and a length of 4 m in UAH's Propulsion Research Center (PRC). For measuring the unsteady forces, the Marsbee robotic flapper was placed in the vacuum chamber, and the pressure and density levels were varied for achieving the Mars atmospheric conditions. The Marsbee flapper generates positive lift in the Earth and Mars conditions [15]. The experimental measurements of lift force generation in Earth and Martian conditions are shown in Fig. 9. It is noticed that in Mars conditions the mean lift force increases between 8 Hz and 14 Hz and then decreases, whereas in Earth conditions, the mean lift force continuously increases with increasing flapping frequency. This result shows that Marsbee is capable of producing a mean lift force in Martian conditions.

4.2. Development of flapping foil underwater vehicle in Titan Conditions based on thunniform modes of fish propulsion

The Titan, visited by Huygens probe in 2005, has a thick atmosphere and three polar lakes of methane and ethane in the northern region of the planet (Fig. 10). The Titan atmosphere consists of mainly Nitrogen, Methane, Argon, and other gases. The Titan atmosphere comprises three main seas: Punga (200 km wide), Kaken Mare (1000 km wide), and Ligea Mare (400 km wide). The cryogenic seas have composition and conditions of (1.5 bar and 92 °K) similar to the Liquefied natural gas (LNG) existing on Earth. The exploration of these cryogenic deep seas is crucial for mankind who are responsible for the depletion of natural fossil fuels on the Earth. In brief, Titan has a thousand times more oil than Earth [27]. The density of seawater on Earth at 25 °C is 1025 kg/m^3, whereas the density of the fluid present in the Titan's seas Kaken mare liquid (ethane) is 650 kg/m^3. The hydrodynamic forces present in the Titan atmosphere are proportional to the ambient fluid density. The low density of the fluids represents a low Reynolds number. The exploration of these planets with conventional surface and underwater vehicles at a low Reynolds number is difficult to operate. This study proposed a new concept of developing surface and underwater vehicles fitted with flapping foil operating in cryogenic conditions. The cryogenic-liquid stability, resistance, propulsion aspects of the vehicle parameters are the same as the design of underwater vehicles in Earth conditions. The estimation of thrust is generally different from the traditional propeller concept. The main objectives of the bio-inspired flapping foil underwater vehicle are to determine the chemical composition of the liquids present in Titan environments. The development of extra-terrestrial ocean underwater vehicles with flapping foil locomotion results in higher propulsive efficiency and greater maneuverability. The NASA Titan conventional submarine and the proposed bio-inspired underwater vehicle fitted with fish

propulsions are shown in Fig. 11. The dimensions of the conventional Titan submarine and bio-inspired Titan underwater vehicle are given in Table 6. The vehicle is fitted with the thunniform mode caudal fin which oscillates in sway and yaw modes. The caudal fin of the bioinspired vehicle produces low turbulence, thereby low energy loss or drag, and hence higher propulsive efficiency and operational endurance for the vehicle.

4.2.1. Biomimetic propulsion mechanisms for Titan conditions

The AUV is vulnerable when fitted with conventional propellers operating in cryogenic liquids of density less than 650 kg/m^3. The conventional propellers operating in Titan conditions are subjected to frigid atmospheres which may result in the propeller blade structural failure, increased chances of cavitation, propeller blade surface erosion, and hull-propeller induced vibrations induced by cavitation, leading to deteriorated performance of the propeller. Hence, the requirement of biomimetic flapping foils appears to be more suitable in the Titan like environment. The flapping foil operates at a much lower frequency compared to that of conventional propellers. Mannam et al. [99] suggested two modes of locomotion for bio-inspired underwater vehicle propulsion such as undulation and thunniform modes (Fig. 12), which may be more suitable for the vehicles in the Titan environment. In undulation mode, aquatic animals swim through the water by the creation of undulations or flag movements with their bodies or caudal fins. The undulations create components of axial thrust force complemented by a rearward force, side forces, and a normal force that is between the forward thrust and side force. The eel fish operating at undulation mode is an efficient swimmer. On the other hand, the tuna using thunniform mode is a fast swimmer. The slender-body fishes (e.g. sea snakes, eels) generate propulsive waves starting from the head to the tail. The thunniform mode is present in high-speed long-distance swimmers. The anticipated major problem for a vehicle with body undulations or flexibility would be inadequate rigid space inside it to house electronic and mechanical components required for its propulsion system and also the items in its payload such as scanners, cameras, transmitters, etc. So, the thunniform propulsion system, where the flexibility is allowed for the caudal fin and maybe the body rear part, is more suitable for the envisaged biomimetically propelled subsurface vehicles in the Titan oceans. In such a case, the above mentioned electro-mechanical components can be accommodated in the non-flexible middle and forward region of the vehicle.

4.2.2. Design methodology for developing underwater vehicle in titan conditions

The design of underwater vehicles for the exploration of ocean worlds on Titan and Europa conditions is similar to Earth's conditions. The following entails the design of hull form, stability parameters, resistance of the underwater vehicles, and estimation of thrust and torque of the flapping foil. This design methodology acts as a benchmark tool for planetary scientists.

Selection of geometry of the hull form.

The geometry of the hull form (Fig. 13) and shapes of the AUV nose (y_n) and tail (y_t) sections are determined, respectively, from Eqs. (5) and (6):

$$y_n = \frac{1}{2}d\left[1 - \left(\frac{l_n - x_n}{l_n}\right)^{n_n}\right]^{\frac{1}{n_n}} \quad \text{and} \qquad (5)$$

$$2y_t = 9.6556x_t^3 - 4.9x_t^2 + 0.05x_t + d, \qquad (6)$$

where d is the diameter of the hull, y_n is the radius of nose (m), y_t is the radius of the tail (m), l_n is the length of the nose, x_n and x_t are the reference length (m) varying from 0 to l_t [100].

Statics and Dynamics of Vehicle.

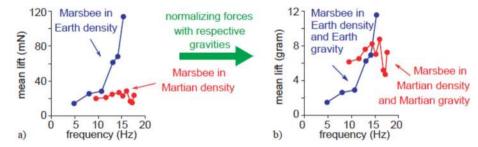Adequate floatation stability for the vehicle is essential in the

Table 5
Comparison of Bumblebee flight on Earth and Mars [15].

Parameters	Bumblebee on Earth	Bumblebee on Mars
Wing size factor	1	1
Atmospheric density, $\rho (kg/m^3)$	1.225	1.55×10^{-2}
Gravitational acceleration (m/s^2)	9.81	3.72
Viscosity coefficient (kg/ms)	1.8×10^{-5}	1.5×10^{-5}
Body mass (kg)	1.75×10^{-4}	1.75×10^{-4}
Total wing area, S (m^2)	1.06×10^{-4}	1.06×10^{-4}
Mass of wings (kg)	9.10×10^{-7}	9.10×10^{-7}
Wing mass/body mass	0.52%	0.52%
Total mass (kg)	1.75×10^{-4}	1.75×10^{-4}
Total weight (mN)	1.72	0.652
Flapping amplitude (deg)	41.6	366
Flapping frequency (Hz)	155	155
Reynolds number	1439	340.6
Wing tip Mach number	0.028	0.33
Aspect ratio	3.3	3.3
Angle of attack	50°	50°
Reduced frequency	0.4054	0.048
Power required (W)	0.012	0.19
Specific power required (W/kg)	68.6	1090
Flapping amplitude less than 90°	Yes	No

Fig. 9. Lift force generation of a Marsbee in (a) Earth and (b) simulated Martian atmospheric conditions [15].
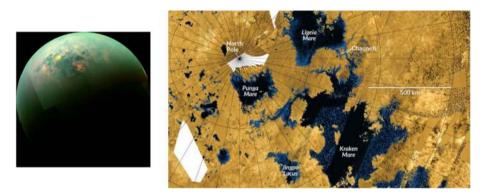

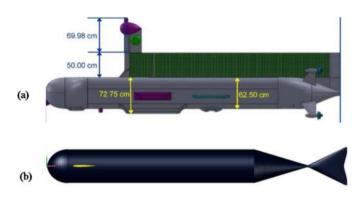**Fig. 10.** Overview of Titan (zoomed-in view: Titan lakes).

Fig. 11. (a) Conventional Titan submarine fitted with thrusters [98]. (b) Proposed bioinspired AUV for Titan [99].

Table 6
Dimensions of underwater vehicles in different conditions.

	Conventional Titan underwater vehicle	Conventional underwater vehicle in Earth's environment	Titan bio-inspired underwater Vehicle
Length	5.883 m	5.781 m	5.781 m
Diameter	0.797 m	0.534 m	0.534 m
Density, ρ	660 kg/m^3	995.6 kg/m^3	660 kg/m^3
Viscosity, ϑ	6.06×10^{-6} Ns/m^2	0.8929×10^{-6} m^2/s	6.06×10^{-6} Ns/m^2
Gravity	1.35 m/s^2	9.81 m/s^2	1.35 m/s^2
Propulsor	Ducted propeller	Screw Propeller	Caudal fin

transverse and longitudinal planes while it is stationary or moving. Different operating conditions such as moving forward, taking a turn, diving, and surfacing, all in liquid and/or icy conditions, should be considered for the vehicle's safety and mission accomplishment. The relevant aspects are discussed below.

Control in the vertical plane: Stability of the AUV in the transverse plane is shown in Fig. 14. The downward force due to the mass multiplied by gravity must be balanced by the upward buoyant force given by the immersed volume multiplied by the water density and gravity. The deeper the vehicle operating at, the greater the water pressure acting on it. It will compress the hull and reduce the immersed volume and hence the upward buoyancy force. Conversely, if the underwater vehicle moves closer to the surface, the water pressure acting on it will be less, and hence the immersed volume and the upward buoyant force will be greater.

Transverse Stability: A submerged vehicle not tending to roll is known as transverse stability. The center of buoyancy (*B*) must be above the center of gravity (*G*), as shown in Fig. 15. In this case, if the boat heels to a small angle, the hydrostatic moment on it will cause it to return to the upright. On the other hand, if the *G* is above *B*, and an external moment causes it to be heeled to a small angle, then the hydrostatic moment will cause it to continue to heel. When it floats on the surface, the situation is different. In this case, the *B* moves transversely when the boat heels. For small angles, the upward force through the *B* always acts through the metacenter (*M*).

Longitudinal Stability: As with transverse stability, the same principles are applied to a submerged vehicle as to a floating surface ship. However, the lack of a water plane results in a very small restoring moment in the longitudinal direction if the vehicle is trimmed, as shown in Fig. 16. Thus, it is essential to have the longitudinal position of the gravity center lined up with the longitudinal position of the center of buoyancy. As the longitudinal position of the gravity center moves during a voyage due to the use of consumables, it is necessary to be able to adjust this by the use of ballast tanks.

Stability when surfacing and diving: When a vehicle is submerged, *BG* is a measure of stability. When the vehicle floats on the surface of water and B moves transversely as a function of the heel through metacenter *M*, the *GM* is a measure of stability similar to surface ships. As a vehicle transits from floating on the water surface to fully submerged, its vertical centers of both buoyancy and gravity will vary, due to a change in the immersion of the hull, and the change in mass in the ballast tanks
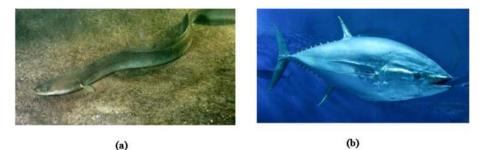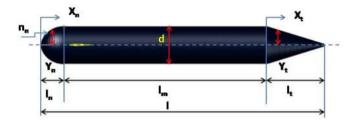
Fig. 12. Propulsive mechanism of (a) eels and (b) Tuna fishes.

Fig. 13. Geometry of hull form.

Fig. 15. (a) Submerged vehicle in transversely stable equilibrium, (b) small heel when B is above G, and (c) heel angle floating on the surface.
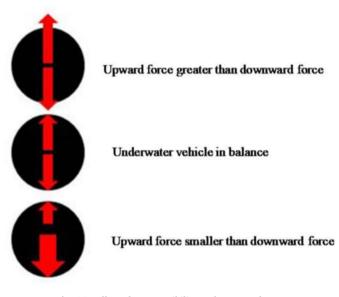

Fig. 14. Effect of compressibility on buoyancy force.

(Fig. 17). In addition, the second moment *I* of the water plane will vary during this process.

Stability when surfacing through ice in Europa conditions: AUVs operating under ice must be able to surface by breaking through the ice. The normal procedure is to stop the AUV under thin ice, and then to slowly surface at zero forward speed (Fig. 18). In Fig. 18, *P* is the upward force, B_F is the position of the center of buoyancy of form displacement, G_F is the position of the center of gravity of form displacement, mg is the vertical downward force through the center of gravity, *bg* is the vertical upward force through the center of buoyancy, *K* is the keel. The initial value of *BG* must be sufficiently high to reduce the instability caused by the force at the top of the sail required to break through the ice.

Resistance Components of AUV in Titan Conditions.

The various components of the resistance include surface friction, form drag, induced drag, and wave-making resistance as shown in Fig. 19. The skin friction resistance is considered as friction on a flat plate with the same wetted surface area at the same *Re*. The frictional form
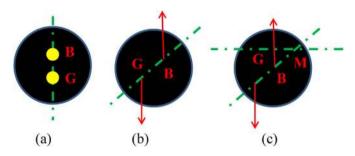
resistance is the difference in frictional resistance between the flow on flat plate and actual flow on submarine. The skin friction and frictional form resistances are together known as the total skin friction. The form drag is viscous pressure resistance caused by the shape of the body [101]. On the other hand, the induced drag is the resistance caused by the appendages. The form drag and induced drag are collectively known as total pressure resistance. The wave-making resistance arises from the generation of surface waves. The effect of reduced gravity on wave-making resistance in Titan conditions is not considered here. If the body travels on or near the free surface, this pressure variation causes waves that radiate away from the body and carry a certain amount of energy that is dissipated in the ocean. The wave-making resistance can then be also characterized by the energy expended by the AUV that is necessary to maintain the wave system. The wave-making resistance only becomes important when the vehicle operates on, or close to, the water surface. The most important difference between the resistances of a surface vessel (or an AUV on the water surface) and a deeply submerged vehicle is that there will be no wave resistance for the latter. Thus, the submerged resistance will be equal to the sum of the above components (Fig. 19).

Procedure for determining the total resistance for autonomous surface vehicle (ASV) in Europa and underwater vehicle (AUV) in Titan condition.

Estimating the total resistance in the Titan condition is crucial for designing propulsors. The propulsor thrust must overwhelm the total resistance. The resistance on the model is scaled to prototype values based on Froude's method of extrapolation using ITTC 78 prediction method [102,103]. In Europa conditions, the atmosphere is the same as the Antarctic sea condition. The ITTC Method and its formulae are valid for water as a fluid, and the empirical relations are based on experiments conducted with a flat plate deeply submerged in water. Hence, the ITTC method is applicable for estimating the resistance of the ASVs operating in icy seas. For this purpose, the flat plate frictional resistance is determined using the ITTC 57 friction correlation line [102,103]. The form factor was obtained by Prohaska's method from low speed towing tests.

(i) **For ASV:** The method of calculation of prototype ASV resistance using model resistance data is:
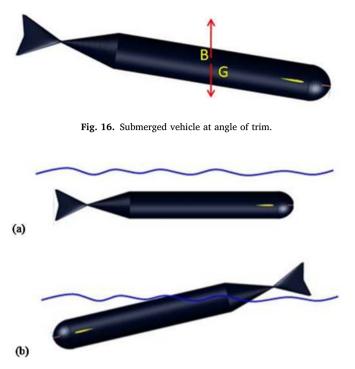
Fig. 16. Submerged vehicle at angle of trim.

(a)

(b)

Fig. 17. (a) Subsurface and (b) diving conditions.
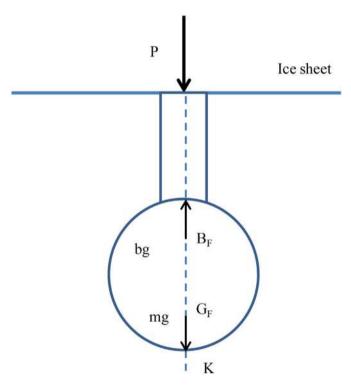

Fig. 18. Underwater vehicle breaking through ice [100].

$R_{TS} = C_{TS} \times 0.5\rho_S \times V_S^2 \times S_S$
$V_S = V_M \sqrt{\lambda}.$
$C_{TS} = C_{FoS} + C_{RS}$
$C_{RS} = C_{RM}$
$C_{RM} = C_{TM} - C_{FoM}$
$C_{TM} = R_{TM} \text{ (N)}/(0.5 \times \rho_{FW} \times V_M^2 \times S_M)$
$C_{FoM} = 0.075/(\log Re_M - 2)^2$
$C_{FoS} = 0.075/(\log Re_S - 2)^2$

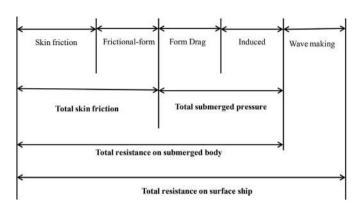Fig. 19. Components of resistance for submerged body.

$$Re_S = V_S L_S / \nu_{SW}$$

$$Re_M = V_M L_M / \nu_{FW} \tag{7}$$

where λ is the geometric scale of the model, R_{TS} is the prototype resistance in Newton, R_{TM} is the model resistance in Newton, V_S is the prototype speed in m/s, V_M is the model speed in m/s, S_S is the wetted surface of the prototype, S_M is the wetted surface of the model, ρ_{SW} is the density of sea water, ρ_{FW} is the density of fresh water, C_{TS} is the coefficient of total resistance of prototype, C_{TM} is the coefficient of total resistance of model, C_{RM} is the residuary resistance coefficient of model, C_{RS} is the residuary resistance coefficient of prototype, C_{FoM} is the coefficient of equivalent flat plate resistance of model, C_{FoS} is the coefficient of equivalent flat plate resistance of prototype, Re_M is the Reynolds number of model, Re_S is the Reynolds number of prototype, L_M is the waterline length of model, L_S is the waterline length of prototype, ν_{FW} is the kinematic viscosity of fresh water for model, ν_{SW} is the kinematic viscosity of sea water for prototype, and $R = (1 + k)$ is the form factor. Following the above scheme, it is possible to extrapolate the model resistance R_{TM} (in Newton) at model speed V_M (in m/s) to prototype resistance R_{TS} (in Newton) at corresponding ship speed V_S.

(ii) **For UV:** The total drag force acting on the AUV body is given by Ref. [103].

$$D = \frac{1}{2}\rho V^2 C_V S \tag{8}$$

where the coefficient of viscous resistance(C_V) for the smooth hull is given by the following equations.

$$C_V = C_F \left[1 + 0.5\left(\frac{d}{l}\right) + 3\left(\frac{d}{l}\right)^3 \right], \text{ and}$$

$$C_V = C_F \left[1 + 0.5\left(\frac{d}{l}\right) + 3\left(\frac{d}{l}\right)^{\left(7 - n_n - \frac{n_t}{2}\right)} \right], \tag{9}$$

d is the diameter of the hull, l is the length of AUV, and n_n and n_t are the effects of nose and tail sections.

Alternative approach: The drag experienced by an axis-symmetric underwater vehicle operating deep below the surface and traveling in a straight line is a direct result of the viscosity effect of the water.

The ITTC 57 correlation line is commonly used in surface ship design to estimate the skin friction (C_F) component of the viscous drag as a function of Re [104].

$$C_F = \frac{0.075}{\left(\log(Re) - 2\right)^2} \tag{10}$$

This is multiplied by a form factor $(1 + k)$ to provide an estimate of the complete viscous drag coefficient. The magnitude of the form factor is

a function of the hull shape. Hoerner [103] proposed the following equation to estimate the form factor for a streamlined body as a function of vessel length (*l*) and diameter (*d*).

$$(1+k) = 1 + 1.5 \left(\frac{d}{l}\right)^{\left(\frac{3}{2}\right)} + 7\left(\frac{d}{l}\right)^3 \quad \text{and} \tag{11}$$

hence, $R_f = C_F \frac{1}{2} \rho S V^2$, $\tag{12}$

where R_f is the frictional resistance in Newton.

(iii) Estimating torque of thunniform caudal fin in bio-inspired AUV in Europa and Titan conditions

The estimation of the power to drive the bio-inspired AUV fitted with caudal fin requires the maximum torque equation given by,

$$Q_{max} = D_{max}r = 2\pi^2 C_D \rho r^3 A_f f^2 sin^2 \psi, \tag{13}$$

where D_{max} is the maximum drag force in Newton, r is the distance between the gravity center and the joint, C_D is the drag force coefficient ($C_D = 1.2$, fin assumed as flat plate), A_f is the fin profile area, and ψ is the yaw angle amplitude [99].

4.3. Estimation of resistance of ice for a flapping foil AUV in Europa conditions

The Antarctic ice sheet overlying unexplored subglacial lakes represents the closest Earth analog for testing advanced Europa missions. As such, the ice sheet provides an extraordinary opportunity for mission simulations, testing of life search protocols and algorithms, and assessing the reliability of various concepts when subjected to long-term operations.

(i) **Lindqvist formula**: This formula was developed from the full-scale tests done in the Bay of Bothnia [105]. The formula is applied to determine the total ice resistance of a surface vessel or underwater vehicle in a surface condition of the ice atmosphere of Europa Moon. The total ice resistance is the sum of bending, crushing, and submerged resistances. The total ice resistance is a function of the ship main dimensions (length *L*, breadth *B*, draft *T*, and speed *S*), hull form, ice strength (σ_b), ice thickness (h_i), and ice friction. The formula is given as:

$$R_{ice} = (R_c + R_b)\left(1 + 1.4\frac{S}{\sqrt{gh_i}}\right) + R_s\left(1 + 9.4\frac{S}{\sqrt{gL}}\right),$$

$$R_c = 0.5 \,\sigma_b h_i^2 \frac{\tan\varnothing + \mu\cos\varnothing/\cos\psi}{1 - \mu\sin\varnothing/\cos\psi},$$

$$R_b = \frac{27}{64}\sigma_b B \frac{h_i^{1.5}}{\sqrt{\dfrac{E}{12(1-v^2)g\rho_w}}} \frac{tan\psi + \mu cos\varnothing}{cos\psi sin\alpha}\left(1 + \frac{1}{cos\psi}\right),$$

$$R_s = (\rho_w - \rho_i)gh_i B\left(T\frac{B+T}{B+2T} + k\right),$$

$$k = \mu\left(0.7L - \frac{T}{\tan\varnothing} - \frac{B}{4tan\alpha} + Tcos\varnothing cos\psi\sqrt{\left(\frac{1}{sin\varnothing^2} + \frac{1}{tan\alpha^2}\right)}\right), \text{ and}$$

$$\varnothing = \arctan\left(\frac{\tan\varnothing}{sin\alpha}\right), \tag{14}$$

where R_{ice}, R_c, R_b, R_s are the total ice resistance, crushing resistance, bending resistance, and submergence resistance. The density of water and ice are denoted by ρ_w and ρ_i. E and υ are Young's modulus and

Poisson's ratio of ice. The μ, ϕ, α, ψ are the coefficient of friction, stem angle, waterline entrance angle, and flare angle, respectively.

(ii) **Keinonen Formula:** This formula is used for determining the ice resistance at low speeds. This formula includes hull dimensions (*L*, *B*, and *T*), hull form, ambient temperatures, and properties of ice. The expression of ice resistance is given below.

$$R_{ice} = C_f\left(0.08 + 0.017C_s C_h B^{0.7}L^{0.2}T^{0.1}H^{1.25}k_1 k_2\right)$$

where $k_1 = (1 - 0.0083(t + 30))(0.63 + 0.00074\sigma_f)$,

$k_2 = (1 - 0.0018(90 - \psi)^{1.4})(1 + 0.04(\phi - 5)^{1.5})$, and

$$C_f = \frac{1 + \dfrac{a}{\sqrt{ghi}}}{1 + \dfrac{a1}{\sqrt{ghi}}}. \tag{15}$$

Here R_{ice} is the total ice resistance, C_s, C_h and C_f are the water salinity, hull coefficient and correction factor, σ_f is the flexural strength and H is the strength of ice, and $\psi \,and\, \phi$ are the flare and buttock angles, respectively [106].

5. Estimation of powering and propulsion of underwater vehicles operating in Titan and Earth conditions

The dimensions of conventional underwater vehicles operating in Titan's and Earth's environments and bio-inspired underwater vehicles operating in Titan's environment are given in Table 6 [107]. The atmospheric density and gravitational parameters presented in Table 6 are used for estimating the resistance and powering performance of underwater vehicles operating in Titan's and Earth's conditions. By using these parameters, the preliminary design of the underwater vehicles can be carried out. The conventional Titan underwater vehicle fitted with thrusters is shown in Fig. 11a. The resistance of the conventional underwater vehicle in Earth's environment is obtained from the towing tank tests. The dimensions of the towing tank are 500 m × 8 m × 8 m. The tank is fitted with a high speed towing carriage which runs at a maximum forward speed of 20 m/s and runs on parallel rails which are fitted to have a tolerance of 0.2 mm. The drag of the Titan bio-inspired underwater vehicle was estimated using the above empirical relations (Eq. (10)) where the fluid properties of Titan's environment are considered in ITTC 1957 formulae.

The resistance and effective power of an underwater vehicle in Titan's and Earth's environments are shown in Fig. 20. The resistance of bare hull (streamlined body) at velocity 1.57 m/s is 14.5 N and 16.3 N in Titan's and Earth's environments, respectively (Fig. 20a and b). The total drag of Titan underwater vehicle fitted with appendages considering the body as a non-streamlined object is 143.68 N at a speed of 1.57 m/s. The effective power of the titan underwater vehicle is 225.5 W at 1.57 m/s (Fig. 20c). The conventional underwater vehicle in the Earth environment is considered as streamlined with no appendages. The total effective power of an underwater vehicle in the Earth environment is 53.35 W at 1.5 m/s (Fig. 20d). The bio-inspired underwater vehicle fitted with caudal fin operating in Titan Environment is shown in Fig. 11b. The drag of the streamlined body fitted with the caudal fin is estimated using Eqs. (10) and (12). Similarly, the resistance of a bio-inspired underwater vehicle operating in Titan's environment is shown in Fig. 21. The estimated drag force acting on a body at a speed of 1.57 m/s is 17.5 N. The thrust performance of a conventional propeller fitted to a Titan submarine is shown in Fig. 22a. The thrust produced against a propeller speed of 900 rpm is 10.7 N. The thrust performance of a bio-inspired underwater vehicle (length = 1 m) fitted with the caudal fin operating in the surface condition is 34.06 N measured at flapping frequency $f = 1.0$ Hz. Similarly, in submerged conditions, the caudal fin produces a thrust of 18.6 N at $f = 0.75$ Hz and is shown in Fig. 22b [108]. The thrust produced by conventional Titan submarine fitted with a ducted propeller is 1/3rd less
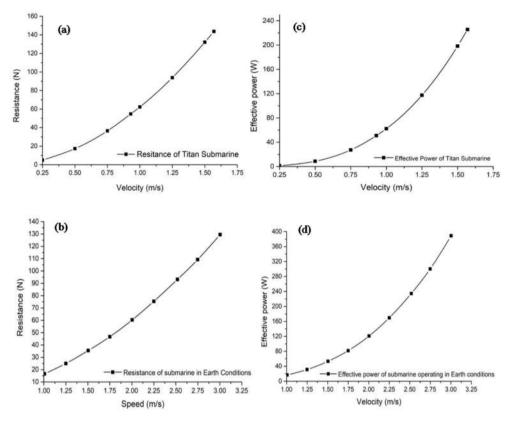
Fig. 20. (a, b) Resistance and (c, d) effective power of submarine operating in Titan's and Earth's environments [98].
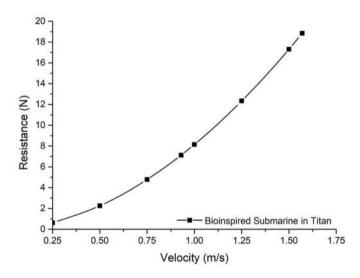

Fig. 21. Resistance of bio-inspired submarine operating in Titan environment [98].

than the submarine operating in Earth's condition due to lower fluid density [107]. It shows that the proposed bio-inspired Titan submarine fitted with the caudal fin will be able to produce sufficient thrust with less power requirements in Titan environment conditions. The Reynolds numbers of different kinds of underwater vehicles in different environments are shown in Fig. 23. The underwater vehicle in Earth's environment is subjected to high *Re* and the vehicles (conventional and bio-inspired) in Titan's environment are subjected to low *Re* because of low fluid densities.

6. Summary and conclusions

The explorations of planets such as Mars, Titan, Europa, Enceladus with the use of aerial, terrestrial, and underwater rovers are gaining significant interest from academia, industry, and international space agencies around the globe. Obtaining scientific knowledge and understanding the environmental conditions of these planets from various space probes are still ongoing. The understanding of planet atmospheres is very important for designing any planetary rovers for future missions. The lack of coordination between the planetary scientists, robotic engineers, and other scientific disciplines hinders the development of efficient planetary rovers, causing various mission failures [109]. The propulsion system for tuna fish, mackerel, whale, and dolphins is up to 80% efficient, while the conventional screw propeller is only 40%–50% efficient. The conventional aerial vehicles fitted with fixed wings or rotary propellers generate insufficient lift in low-density atmospheres. The selection of suitable propulsion mechanism is challenging in the design of planetary rovers. The insect and fish locomotion provides an alternative propulsion mechanism to the planetary rovers. This review article attempts to study the planetary atmospheres and their fluidic conditions for developing the aerial and underwater rovers based on insects and fish locomotion. The Kraken Mare Sea on Titan has a spread of 1170 km in width and an estimated depth of 300 m, and the size is similar to that of the Caspian sea. The Ligeia Mare Lake on Titan measures 500 km in width. It is the suggested site for landing on Titan. The atmospheric density on Mars is only 1.3% of Earth's atmospheric density. This low-density atmosphere on Mars reduces the operational Reynolds number to 10^2-10^3 for fixed-wing and rotary aircraft which produces insufficient lift. The Reynolds number of Titan submarine is 10^5 while the conventional submarine Reynolds number is 10^9 on Earth. Insects have been flying efficiently on both Earth and Mars, using low Reynolds number unsteady aerodynamics. The insect-inspired vehicles should thus be considered on Mars.

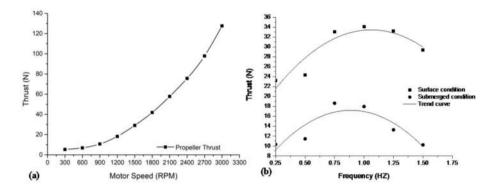We applied the classical aerodynamic and hydrodynamic theories,

Fig. 22. (a) Thrust performance of propeller operating in Titan environment [107]. (b) Thrust performance of bioinspired submarine in Earth's environment [108].
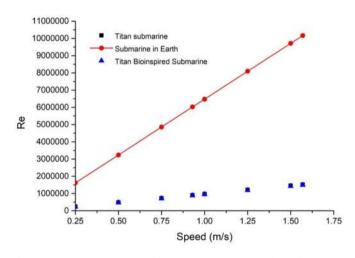

Fig. 23. Effect of speed on Reynolds number in Titan and Earth conditions [98].

used in conventional aerial and underwater vehicle design for earth, to the initial design of planetary bodies. The review presents the detailed design and analysis of flapping flight propulsion in the conditions of Earth and other planetary bodies outside the solar system, such as Mars, Jupiter's moon Europa and Saturn's moons Enceladus and Titan. The environmental conditions and the parameters governing the application of flapping foils in those planetary bodies are outlined. The aerodynamic forces acting on flapping wings in both Earth and Mars conditions are compared. The flapping wings are designed for Mars atmospheric conditions and experimented in a vacuum chamber facility where the temperature and pressure conditions are variable. The results show the flapping wings in Mars conditions can produce sufficient lift forces, given the vehicle weight in Mars atmospheric conditions. Similarly, the design of bio-inspired underwater vehicles based on tuna and eel fishes are studied and proposed for Titan. The hydrodynamic aspects such as the geometry of hull form, resistance and powering, stability characteristics of the vehicles are presented in this article. The comparative analysis of resistance and powering of Titan conventional submarine and Titan bio-inspired underwater vehicles based on hydrodynamic theories are carried out and presented. This analysis is based on the Titan atmospheric conditions. The design of autonomous surface vehicles based on Europa conditions is presented. The Europa atmospheric conditions are similar to the Antarctic conditions. This paper provides sufficient literature about the planetary bodies and their characteristics outside the solar system. The design methodologies and hydrodynamics aspects used in this article act as a benchmark tool for future missions on Mars, Titan, Europa, and Enceladus for the scientific community.

Declaration of competing interest

The authors declare that they have no known competing financial interests or personal relationships that could have appeared to influence the work reported in this paper.

References

[1] M.M. Alam, Z. Muhammad, Dynamics of flow around a pitching hydrofoil, J. Fluid Struct. 99 (2020) 103151.
[2] M.S. Triantafyllou, F.S. Hover, A.H. Techet, D.K. Yue, Review of hydrodynamic scaling laws in aquatic locomotion and fishlike swimming, Appl. Mech. Rev. 58 (2005) 226–237.
[3] J.J. Prabhu, V. Nagarajan, M.R. Sunny, O.P. Sha, On the fluid-structure interaction of a marine cycloidal propeller, Appl. Ocean Res. 64 (2017) 105–127.
[4] S.C. Misra, R.P. Gokarn, O.P. Sha, C. Suryanarayana, R.V. Suresh, Development of a four-bladed surface piercing propeller series, Nav. Eng. J. 124 (4) (2012) 105–138.
[5] S. Susan, D. Wardhani, Building integrated photovoltaic as GREENSHIP'S on site renewable energy tool, Results Eng. 7 (2020) 100153.
[6] Aldehayyat Yazan, Richard Dahan, Iman Fayyad, Jean Martin, Matthew Perkins, Rachel Sharples, Ocra-xi: an Autonomous Underwater Vehicle, OCRA AUV Team, 2009. http://web.mit.edu/ocra.
[7] G. Griffiths, I. Edwards, AUVs: Designing and Operating Next-Generation Vehicles, vol. 69, Elsevier Oceanography Series, 2003, pp. 229–236.
[8] K.A. Morgansen, B.I. Triplett, D.J. Klein, Geometric methods for modeling and control of free-swimming fin-actuated underwater vehicles, IEEE Trans. Robot. 23 (6) (2007) 1184–1199.
[9] H. Hu, J. Liu, I. Dukes, G. Francis, Design of 3D swim patterns for autonomous robotic fish, in: Intelligent Robots and Systems, 2006 IEEE/RSJ International Conference on, IEEE, 2006, October, pp. 2406–2411.
[10] J. Yu, L. Wang, Parameter optimization of simplified propulsive model for biomimetic robot fish, in: Robotics and Automation, 2005. ICRA 2005. Proceedings of the 2005 IEEE International Conference on, IEEE, 2005, pp. 3306–3311.
[11] G.D. Weymouth, Biologically Inspired Force Enhancement for Maritime Propulsion and Maneuvering, 2016 arXiv preprint arXiv:1609.06559.
[12] B. Huang, A. Ducoin, Y.L. Young, Physical and numerical investigation of cavitating flows around a pitching hydrofoil, Phys. Fluids 25 (10) (2013) 102109.
[13] A. Boudis, A. Benzaoui, H. Oualli, O. Guerri, A.C. Bayeul-Lainé, O. Coutier-Delgosha, Energy Extraction Performance Improvement of a Flapping Foil by the Use of Combined Foil, 2018.
[14] M. Ono, K. Carpenter, M.L. Cable, B.H. Wilcox, L.P. Tosi, Exobiology extant life surveyor (EELS). AGU Fall Meeting 2019, AGU, 2019, December.
[15] C.K. Kang, F. Fahimi, R. Griffin, D.B. Landrum, B. Mesmer, G. Zhang, T. Lee, H. Aono, J. Pohly, J. McCain, M. Sridhar, Marsbee-swarm of flapping wing flyers for enhanced mars exploration, in: Phase I: Final Report; NASA Innovative Advanced Concepts (NIAC), 2019.
[16] Jacob Samuel Izraelevitz, Flapping Wings for Dual Aerial and Aquatic Propulsion, Diss. Massachusetts Institute of Technology, 2017.
[17] Y. Chen, E.F. Helbling, N. Gravish, K. Ma, R.J. Wood, Hybrid aerial and aquatic locomotion in an at-scale robotic insect, in: 2015 IEEE/RSJ International Conference on Intelligent Robots and Systems (IROS), IEEE, 2015, December, pp. 331–338.

[18] B. Zhu, P. Xia, Y. Huang, W. Zhang, Energy extraction properties of a flapping wing with an arc-deformable airfoil, J. Renew. Sustain. Energy 11 (2) (2019), 023302.

[19] J.A. Bowker, N.C. Townsend, M. Tan, R.A. Shenoi, Experimental analysis of submerged flapping foils; implications for autonomous surface vehicles (ASVs), in: OCEANS 2016 MTS/IEEE Monterey, IEEE, 2016, September, pp. 1–10.

[20] E. Bøckmann, S. Steen, Model test and simulation of a ship with wavefoils, Appl. Ocean Res. 57 (2016) 8–18.

[21] S. Pieterkosky, A. Ziegwied, C. Cavanagh, L. Thompson, September). BIV meets ASV: bio-inspired fish drones and autonomous surface vehicles for coral reef monitoring, in: OCEANS 2017-Anchorage, IEEE, 2017, pp. 1–5.

[22] F.Z. Temel, S. Yesilyurt, April). Magnetically actuated micro swimming of bio-inspired robots in mini channels, in: 2011 IEEE International Conference on Mechatronics, IEEE, 2011, pp. 342–347.

[23] M.S. Triantafyllou, G.S. Triantafyllou, An efficient swimming machine, Sci. Am. 272 (3) (1995) 64–70.

[24] J.M. Anderson, N.K. Chhabra, Maneuvering and stability performance of a robotic tuna, Integr. Comp. Biol. 42 (1) (2002) 118–126.

[25] J. Liu, H. Hu, A 3D simulator for autonomous robotic fish, Int. J. Autom. Comput. 1 (1) (2004) 42–50.

[26] A.R. Hendrix, T.A. Hurford, L.M. Barge, M.T. Bland, J.S. Bowman, W. Brinckerhoff, B.J. Buratti, M.L. Cable, J. Castillo-Rogez, G.C. Collins, S. Diniega, The NASA roadmap to ocean worlds, Astrobiology 19 (1) (2019) 1–27.

[27] Ralph Lorenz, Karl Mitchell, Randolph Kirk, Alexander Hayes, Oded Aharonson, Howard Zebker, Philippe Paillou, Jani Radebaugh, Jonathan Lunine, M. Janssen, Steve Wall, Rosaly Lopes, Bryan Stiles, Steve Ostro, Giuseppe Mitri, Ellen Stofan, Titan's inventory of organic surface materials, Geophys. Res. Lett. 35 (2008), https://doi.org/10.1029/2007GL032118.

[28] H. Morikawa, S. Nakao, S.I. Kobayashi, Experimental study on the oscillating wing for propulsor with bending mechanism modeled on the caudal muscle-skeletal structure of tuna, JSME Int. J. - Ser. C Mech. Syst. Mach. Elem. Manuf. Q. 44 (4) (2001) 1117–1124.

[29] H. Dewar, J. Graham, Studies of tropical tuna swimming performance in a large water tunnel-Energetics, J. Exp. Biol. 192 (1) (1994) 13–31.

[30] M.M. Koochesfahani, Vortical patterns in the wake of an oscillating airfoil, AIAA J. 27 (9) (1989) 1200–1205.

[31] K.D. Jones, C.M. Dohring, M.F. Platzer, Wake structures behind plunging airfoils: a comparison of numerical and experimental results, AIAA Paper 78 (1996) 1996.

[32] O. Haugsdal, Motion control of oscillating foils for steady propulsion and starting maneuvers, in: Master of Science in Ocean Engineering, Massachusetts Institute of Technology, Massachusetts, USA, 2000.

[33] A. Das, R.K. Shukla, R.N. Govardhan, Existence of a sharp transition in the peak propulsive efficiency of a low-Re pitching foil, J. Fluid Mech. 800 (2016) 307–326.

[34] J. Walker, M. Westneat, Labriform propulsion in fishes: kinematics of flapping aquatic flight in the bird wrasse Gomphosusvarius (Labridae), J. Exp. Biol. 200 (11) (1997) 1549–1569.

[35] L. Schouveiler, F.S. Hover, M.S. Triantafyllou, Performance of flapping foil propulsion, J. Fluid Struct. 20 (7) (2005) 949–959.

[36] K.N. Lucas, P.J. Thornycroft, B.J. Gemmell, S.P. Colin, J.H. Costello, G.V. Lauder, Effects of non-uniform stiffness on the swimming performance of a passively-flexing, fish-like fish model, Bioinspiration Biomimetics 10 (5) (2015), 056019.

[37] N.P.B. Mannam, P. Krishnankutty, H. Vijayakumaran, R.C. Sunny, Experimental and numerical study of penguin mode flapping foil propulsion system for ships, JBE 14 (2017) 770–780.

[38] H. Morikawa, A. Hiraki, S. Kobayashi, Y. Muguruma, Outboard Propulsor with an Oscillating Horizontal Fin. Bio-Mechanisms of Swimming and Flying, Springer, Tokyo, 2002, pp. 67–78.

[39] J.R. Gottlieb, J.L. Tangorra, C.J. Esposito, G.V. Lauder, A biologically derived pectoral fin for yaw turnmaneuvers, Appl. Bionics Biomechanics 7 (1) (2010) 41–55.

[40] G.V. Lauder, P.G.A. Madden, J.L. Tangorra, E. Anderson, T.V. Baker, Bioinspiration from fish for smart material design and function, Smart Mater. Struct. 20 (9) (2011), 094014.

[41] S.Y. Shinde, J.H. Arakeri, Flexibility in flapping foil suppresses meandering of the induced jet in absence of free stream, J. Fluid Mech. 757 (2014) 231–250.

[42] J.D. Young, S.E. Morris, R.R. Schutt, C.H.K. Williamson, Effect of hybrid-heave motions on the propulsive performance of an oscillating airfoil, J. Fluid Struct. 89 (2019) 203–218.

[43] K.B. Lua, H. Lu, X.H. Zhang, T.T. Lim, K.S. Yeo, Aerodynamics of two-dimensional flapping wings in a tandem configuration, Phys. Fluids 28 (12) (2016) 121901.

[44] James A. Bowker, Coupled Dynamics of a Flapping Foil Wave Powered Vessel, University of Southampton, Doctoral Thesis, 2018, p. 251.

[45] K. Carpenter, M. Cable, NASA Eel Robots. Exobiology Extant Life Surveyor or EELS Robot Architecture, 2019. https://www.youtube.com/watch?v=7bdS_xpYz7A&t=186s.

[46] J. Ayers, C. Wilbur, C. olcott,«Lamprey robots», in: International Symposium on Aqua Biomechanisms, 2000.

[47] Yu, Y. Hu, R. Fan, L. Wang, J. Huo, Mechanical design and motion control of a biomimetic robotic dolphin, Adv. Robot. 21 (3-4) (2007) 499–513.

[48] L.A. van Duren, E.J. Stamhuis, J.J. Videler, Copepod feeding currents: flow patterns, filtration rates, and energetics, J. Exp. Biol. 206 (2) (2003) 255–267.

[49] U.K. Müller, B.L.E. Van Den Heuvel, E.J. Stamhuis, J.J. Videler, Fish footprints: morphology and energetics of the wake behind a continuously swimming mullet (ChelonlabrosusRisso), J. Exp. Biol. 200 (22) (1997) 2893–2906.

[50] M.J. Wolfgang, J.M. Anderson, M.A. Grosenbaugh, D.K. Yue, M.S. Triantafyllou, Near-body flow dynamics in swimming fish, J. Exp. Biol. 202 (17) (1999) 2303–2327.

[51] W.O.L.F. Hanke, C. Brucker, H.O.R.S.T. Bleckmann, The ageing of the low-frequency water disturbances caused by swimming goldfish and its possible relevance to prey detection, J. Exp. Biol. 203 (7) (2000) 1193–1200.

[52] J. Sakakibara, M. Nakagawa, M. Yoshida, Stereo-PIV study of flow around a maneuvering fish, Exp. Fluid 36 (2) (2004) 282–293.

[53] K. Matsuuchi, T. Miwa, T. Nomura, J. Sakakibara, H. Shintani, B.E. Ungerechts, Unsteady flow field around a human hand and propulsive force in swimming, J. Biomech. 42 (1) (2009) 42–47.

[54] E.D. Tytell, G.V. Lauder, The hydrodynamics of eel swimming, J. Exp. Biol. 207 (11) (2004) 1825–1841.

[55] D.R. Warrick, B.W. Tobalske, D.R. Powers, Aerodynamics of the hovering hummingbird, Nature 435 (7045) (2005) 1094.

[56] G.V. Lauder, Swimming hydrodynamics: ten questions and the technical approaches needed to resolve them, Exp. Fluid 51 (1) (2009) 23–35.

[57] B.E. Flammang, G.V. Lauder, Functional morphology and hydrodynamics of backward swimming in bluegill sunfish, Lepomis macrochirus, Zoology 119 (5) (2016) 414–420.

[58] V. Mwaffo, P. Zhang, S.R. Cruz, M. Porfiri, Zebrafish swimming in the flow: a particle image velocimetry study, PeerJ 5 (2017), e4041.

[59] L. Wang, M.M. Alam, Y. Zhou, Experimental Study of a Passive Control of Airfoil Lift Using Bioinspired Feather Flap, *Bioinspiration & Biomimetics*14, 2019, 066005, 1-14.

[60] K. Muramatsu, J. Yamamoto, T. Abe, K. Sekiguchi, N. Hoshi, Y. Sakurai, Oceanic squid do fly, Mar. Biol. 160 (5) (2013) 1171–1175.

[61] R.J. Lock, R. Vaidyanathan, S.C. Burgess, June. Design and experimental verification of a biologically inspired multi-modal wing for aerial-aquatic robotic vehicles, in: 2012 4th IEEE RAS & EMBS International Conference on Biomedical Robotics and Biomechatronics (BioRob), IEEE, 2012, pp. 681–687.

[62] Y. Chen, H. Wang, E.F. Helbling, N.T. Jafferis, R. Zufferey, A. Ong, R.J. Wood, A biologically inspired, flapping-wing, hybrid aerial-aquatic microrobot, Sci. Robot. 2 (11) (2017), eaao5619.

[63] M. Krieg, K. Nelson, J. Eisele, K. Mohseni, Bioinspired jet propulsion for disturbance rejection of marine robots, IEEE Robot. Autom. Lett. 3 (3) (2018) 2378–2385.

[64] R. Sullivan, R. Greeley, M. Kraft, G. Wilson, M. Golombek, K. Herkenhoff, J. Murphy, P. Smith, Results of the imager for mars pathfinder windsock experiment, J. Geophys. Res.: Plan 105 (E10) (2000) 24547–24562.

[65] J.S. Levine, M.A. Croom, H.S. Wright, B.D. Killough, W.C. Edwards, The Aerial Regional-Scale Environmental Surveyor (ARES): New Mars Science to Reduce Human Risk and Prepare for the Human Exploration, 2012.

[66] C.A. Kuhl, Mars Aerial Regional-Scale Environmental Survey (ARES) Coordinate Systems Definitions and Transformations, 2009.

[67] R.D. Braun, H.S. Wright, M.A. Croom, J.S. Levine, D.A. Spencer, Design of the ARES Mars airplane and mission architecture, J. Spacecraft Rockets 43 (5) (2006) 1026–1034.

[68] H. Wright, M. Croom, R. Braun, G. Qualls, P. Cosgrove, J. Levine, ARES mission overview-Capabilities and requirements of the robotic aerial platform, in: 2nd AIAA" Unmanned Unlimited" Conf. and Workshop & Exhibit, 2003, p. 6577.

[69] S. Sandford, M. Croom, R. Moses, C. Kuhl, M. Guynn, R. Braun, J. Levine, J. Langford, September). Ares and beyond: autonomous aerial platforms provide a unique measurement capability for earth and planetary science. AIAA" Unmanned Unlimited" Conf. And Workshop & Exhibit, 2003, p. 6610.

[70] J. Levine, D. Blaney, J.E.P. Connemey, R. Greeley, J. Head III, J. Hoffman, B. Jakosky, C. McKay, C. Sotin, M. Summers, Science from a mars airplane: the aerial regional-scale environmental survey (ARES) of mars, in: AIAA" Unmanned Unlimited" Conf. and Workshop & Exhibit, 2003, p. 6576.

[71] A.J.R. Lopez-Arreguin, S. Montenegro, Improving engineering models of terramechanics for planetary exploration, Results Eng. 3 (2019) 100027.

[72] R.M. Zubrin, June). The mars gashopper, in: Concepts and Approaches for Mars Exploration, vol. 1679, 2012.

[73] M.N. Thornblom, J.N. Lukas, R.A. Lugo, June). Systematic and widespread exploration with aerocoasting and reconnaissance of the martian sub-atmosphere (swarms), in: Concepts and Approaches for Mars Exploration, vol. 1679, 2012.

[74] A. Wolf, L. Beegle, C. Raymond, J. Plaut, B. Pollard, Y. Gim, X. Wu, J. Hall, Mars balloon science, in: Concepts and Approaches for Mars Exploration, vol. 1679, 2012, June.

[75] J. Hall, M. Pauken, V. Kerzhanovich, G. Walsh, E. Kulczycki, D. Fairbrother, C. Shreves, T. Lachenmeier, Mars balloon flight test results, in: AIAA Balloon Systems Conference, 2009, p. 2809.

[76] B. Balaram, T. Canham, C. Duncan, H.F. Grip, W. Johnson, J. Maki, A. Quon, R. Stern, D. Zhu, Mars helicopter technology demonstrator, in: 2018 AIAA Atmospheric Flight Mechanics Conference, 2018, p. 23.

[77] G.J. Berman, Z.J. Wang, Energy-minimizing kinematics in hovering insect flight, J. Fluid Mech. 582 (2007) 153–168.

[78] I. Faruque, J.S. Humbert, Dipteran insect flight dynamics. Part 1 Longitudinal motion about hover, J. Theor. Biol. 264 (2) (2010) 538–552.

[79] A. Ania, D. Poirel, M.J. Potvin, S. Montminy, Flapping wing devices for mars exploration, in: Proceedings of the Canadian Engineering Education Association (CEEA), 2004.

[80] X. Cheng, M. Sun, Wing-kinematics measurement and aerodynamics in a small insect in hovering flight, Sci. Rep. 6 (2016) 25706.

[81] J. Brandt, G. Doig, N. Tsafnat, Computational aerodynamic analysis of a micro-CT based bio-realistic fruit fly wing, PloS One 10 (5) (2015), e0124824.

[82] R. Noda, T. Nakata, H. Liu, Effects of wing deformation on aerodynamic performance of a revolving insect wing, Acta Mech. Sin. 30 (6) (2014) 819–827.

[83] A. Vargas, R. Mittal, H. Dong, A computational study of the aerodynamic performance of a dragonfly wing section in gliding flight, Bioinspiration Biomimetics 3 (2) (2008), 026004.

[84] X.G. Meng, M. Sun, Aerodynamic effects of wing corrugation at gliding flight at low Reynolds numbers, Phys. Fluids 25 (7) (2013), 071905.

[85] X.L. Mou, Y.P. Liu, M. Sun, Wing motion measurement and aerodynamics of hovering true hoverflies, J. Exp. Biol. 214 (17) (2011) 2832–2844.

[86] M. Sun, S.L. Lan, A computational study of the aerodynamic forces and power requirements of dragonfly (Aeschna juncea) hovering, J. Exp. Biol. 207 (11) (2004) 1887–1901.

[87] W. Shyy, H. Aono, S.K. Chimakurthi, P. Trizila, C.K. Kang, C.E. Cesnik, H. Liu, Recent progress in flapping wing aerodynamics and aeroelasticity, Prog. Aero. Sci. 46 (7) (2010) 284–327.

[88] M.R. Amiralaei, H. Alighanbari, S.M. Hashemi, Flow field characteristics study of a flapping airfoil using computational fluid dynamics, J. Fluid Struct. 27 (7) (2011) 1068–1085.

[89] M.A. Fenelon, T. Furukawa, Design of an active flapping wing mechanism and a micro aerial vehicle using a rotary actuator, Mech. Mach. Theor. 45 (2) (2010) 137–146.

[90] T. Fujikawa, K. Hirakawa, S. Okuma, T. Udagawa, S. Nakano, K. Kikuchi, Development of a small flapping robot: motion analysis during takeoff by numerical simulation and experiment, Mech. Syst. Signal Process. 22 (6) (2008) 1304–1315.

[91] G. Du, M. Sun, Effects of wing deformation on aerodynamic forces in hovering hoverflies, J. Exp. Biol. 213 (13) (2010) 2273–2283.

[92] X.G. Meng, L. Xu, M. Sun, Aerodynamic effects of corrugation in flapping insect wings in hovering flight, J. Exp. Biol. 214 (3) (2011) 432–444.

[93] D.E. Levy, A. Seifert, Parameter study of simplified dragonfly airfoil geometry at Reynolds number of 6000, J. Theor. Biol. 266 (4) (2010) 691–702.

[94] H.V. Phan, Q.V. Nguyen, Q.T. Truong, T. Van Truong, H.C. Park, N.S. Goo, M.J. Kim, Stable vertical takeoff of an insect-mimicking flapping-wing system without guide implementing inherent pitching stability, JBE 9 (4) (2012) 391–401.

[95] C.T. Orlowski, A.R. Girard, Modeling and simulation of nonlinear dynamics of flapping wing micro air vehicles, AIAA J. 49 (5) (2011) 969–981.

[96] M. Sun, J.K. Wang, Flight stabilization control of a hovering model insect, J. Exp. Biol. 210 (15) (2007) 2714–2722.

[97] M. Sun, Y. Xiong, Dynamic flight stability of a hovering bumblebee, J. Exp. Biol. 208 (3) (2005) 447–459.

[98] S.R. Oleson, R. Lorenz, M. Paul, Titan submarine: exploring the depths of kraken mare, in: AIAA SPACE 2015 Conference and Exposition, 2015, p. 4445.

[99] N.P.B. Mannam, P. Krishnankutty, Hydrodynamic study of flapping foil propulsion system fitted to surface and underwater vehicles, Ships Offshore Struct. 13 (6) (2018) 575–583.

[100] M. Renilson, Submarine Hydrodynamics, Springer, Launceston, Australia, 2015, pp. 45–89.

[101] C.J. Ejeh, G.P. Akhabue, E.N. Boah, K.K. Tandoh, Evaluating the influence of unsteady air density to the aerodynamic performance of a fixed wind aircraft at different angle of attack using computation fluid dynamics, Results Eng. 4 (2019) 100037.

[102] J. Feldman, DTNSRDC Revised Standarrd Submarine Equations of Motion (No. DTNSRDC/SPD-0393-09), David W Taylor Naval Ship Research and Development Center Bethesda MD Ship Performance Dept, 1979.

[103] S.F. Hoerner, Fluid-dynamic drag: practical information on aerodynamic drag and hydrodynamic resistance, Aeronaut. J. 80 (788) (1965) 371.

[104] J. McKevitt, Multiphysics Feasibility Study of an Aerial-Aquatic Spacecraft's Plunge into Kraken Mare (No. EPSC2020-816), Copernicus Meetings, 2020.

[105] G. Lindqvist, A straightforward method for calculation of ice resistance of ships, in: Proceedings of the 10th International Conference on Port and Ocean Engineering under Arctic Conditions (POAC), 1989, pp. 722–735.

[106] J. Hu, L. Zhou, Further study on level ice resistance and channel resistance for an icebreaking vessel, Int. J. Nav. Architect. Ocean. Eng. 8 (2) (2016) 169–176.

[107] S.R. Oleson, R.D. Lorenz, M.V. Paul, Phase 1 Final Report: Titan Submarine, 2015.

[108] N.P.B. Mannam, P. Krishnankutty, Biological Propulsion Systems for Ships and Underwater Vehicles, Propulsion Systems, Alessandro Serpi and Mario Porru, IntechOpen, October 7th 2019, https://doi.org/10.5772/intechopen.82830.

[109] Jon Nelson, Mars Exploration Rover - Spirit". NASA, 2014. Retrieved February 2, 2014.

[112] Y. Lian, T. Broering, K. Hord, R. Prater, The characterization of tandem and corrugated wings, Prog. Aero. Sci. 65 (2014) 41–69.

[113] N.P.B. Mannam, J.M. Mallikarjuna, P. Krishnankutty, Hydrodynamic study of freely swimming shark fish propulsion for marine vehicles using 2D particle image velocimetry, Robot. Biomimetics 3 (1) (2016) 3.

[114] L. Ristroph, S. Childress, Stable hovering of a jellyfish-like flying machine, J. R. Soc. Interface 11 (92) (2014) 20130992.

[115] T. Salume, Design of a Compliant Underwater Propulsion Mechanism by Investigating and Mimicking the Body a Rainbow Trout (oncorhynchus Mykiss), Master's thesis, Tallinn University of Technology, 2010.

[116] J.T. Hrynuk, D.G. Bohl, The effects of leading-edge tubercles on dynamic stall, J. Fluid Mech. 893 (2020).